J. Fluid Mech. (1990), *vol.* 216, *pp.* 343–380
Printed in Great Britain

Resonantly excited regular and chaotic motions in a rectangular wave tank

By WU-TING TSAI[1], DICK K. P. YUE[1]
AND KENNETH M. K. YIP[2]

[1] Department of Ocean Engineering, Massachusetts Institute of Technology,
Cambridge, MA 02139, USA

[2] Department of Electrical Engineering and Computer Science, Massachusetts Institute of
Technology, Cambridge, MA 02139, USA

(Received 23 May 1989 and in revised form 14 December 1989)

We consider the resonant excitation of surface waves inside a rectangular wave tank of arbitrary water depth with a flap-type wavemaker on one side. Depending on the length and width of the tank relative to the sinusoidal forcing frequency of the wave paddle, three classes of resonant mechanisms can be identified. The first two are the well-known synchronous, resonantly forced longitudinal standing waves, and the subharmonic, parametrically excited transverse (cross) waves. These have been studied by a number of investigators, notably in deep water. We rederive the governing equations and show good comparisons with the experimental data of Lin & Howard (1960). The third class is new and involves the simultaneous resonance of the synchronous longitudinal and subharmonic cross-waves and their internal interactions. In this case, temporal chaotic motions are found for a broad range of parameter values and initial conditions. These are studied by local bifurcation and stability analyses, direct numerical simulations, estimations of the Lyapunov exponents and power spectra, and examination of Poincaré surfaces. To obtain a *global* criterion for widespread chaos, the method of resonance overlap (Chirikov 1979) is adopted and found to be remarkably effective.

1. Introduction

The resonantly excited, longitudinal forced waves and transverse cross-waves (wave motions respectively perpendicular and parallel to the wavemaker) in a short wave tank with deep water were investigated both analytically and experimentally by Lin & Howard (1960). Using a method similar to Penney & Price (1952), they looked for periodic nonlinear solutions for the longitudinal and transverse standing waves. For the longitudinal forced standing waves, they obtained a relationship for the response amplitude versus excitation frequency up to third order in surface displacement, a result which was largely confirmed by their experimental measurements. For the standing cross-waves, however, they were able to carry out the analysis only to second order. The nonlinear dependence of the wave amplitude on frequency did not appear, and they were unable to make quantitative comparisons with the experiments.

Since then, there have been two main studies of standing cross-waves in a short wave tank. Garrett (1970) was apparently the first to show that the mechanism for the excitation of transverse cross-waves is indeed a parametric resonance. Using an averaging over the longitudinal waves, Garrett obtained a Mathieu equation governing the amplitude of cross-waves. This analysis explains the occurrence of subharmonic resonant cross-waves at specific excitation frequencies but cannot predict their amplitudes, since the solution of the Mathieu equation is unbounded in the unstable region. Recently, Miles (1988) used a Lagrangian formulation and obtained a Hamiltonian system governing the slow modulation of the cross-wave amplitude. Miles' analysis included the nonlinear interaction between the motion of the wavemaker and the cross-wave to second order and the self-interaction of cross-waves to third order. The equation is equivalent to that governing the parametrically excited surface waves in a vertically oscillating tank (Miles 1984*a*).

Both Garrett's and Miles' studies are for the case where the longitudinal wave is not resonantly excited by the wavemaker. For such conditions, the amplitude of the longitudinal wave is of higher order than that of the resonant cross-wave. If the length of the tank is such that the longitudinal waves are also resonated (synchronously), the amplitudes of both the longitudinal and cross-waves may be of the same order of magnitude (see, for example, the experimental measurements in figure 7.2 of Lin & Howard 1960). In this case, the internal interactions between the two standing waves also become important, resulting in a complicated and varied dynamical system.

In this paper, we re-examine the resonantly excited longitudinal and transverse waves in a three-dimensional rectangular tank with a harmonically driven wavemaker on one side. Depending on the length and width of the tank relative to the forcing frequency and water depth, i.e., on the degree of longitudinal (synchronous) and transverse (subharmonic) turning, the different possible orders of magnitudes of the longitudinal and transverse wave amplitudes relative to that of the paddle are systematically considered. Specifically, the following three sets of ordering are identified:

	Wavemaker	Longitudinal wave	Transverse wave
Case I	$O(\epsilon)$	$O(\epsilon^{\frac{1}{3}})$	$O(\epsilon^{\frac{2}{3}})$
Case II	$O(\epsilon)$	$O(\epsilon)$	$O(\epsilon^{\frac{1}{2}})$
Case III	$O(\epsilon)$	$O(\epsilon^{\frac{1}{2}})$	$O(\epsilon^{\frac{1}{2}})$

where $\epsilon = a/L \ll O(1)$ is the non-dimensional amplitude of the wavemaker motion normalized by the length, L, of the tank. We remark that other order-of-magnitude orderings are in principle possible, for example the somewhat 'obvious' choice of $O(\epsilon^{\frac{1}{3}})$ for both the longitudinal and cross-waves for Case III. With that ordering, however, the requisite coupling occurs only at fifth order and the interactions between forced and parametric resonances are at higher order than the present case.

Case I corresponds to the case where the driving frequency of the wavemaker approximates a natural frequency of the longitudinal standing waves but is not close to twice that of a standing cross-wave. The longitudinal standing wave is synchronously forced and resonated while the cross-wave is not resonant and is of higher order in amplitude. Case II is the opposite situation where the subharmonic cross-waves only are parametrically resonated. The longitudinal waves are not close to resonance, are of higher order, and do not affect the transverse wave motion in this case, as shown by Garrett (1970). The relevant evolution equations governing the amplitudes of the resonant waves for these two cases can be derived using the method of multiple scales. The derivation and results for both cases (§§3 and 4) are similar to a number of existing results for related problems. For the cross-wave Case II, our equation is isomorphic to that of Miles (1988) using the method of averaged

Lagrangian. Interestingly, our results for the more straightforward Case I appear to have been obtained in the present context using multiple scales for the first time. In order to make comparisons to experiments, we consider general finite water depth and *no* approximation is used for the shape function of the wavemaker motion, in contrast to the existing analyses of Lin & Howard (1960) and Miles (1988). In both Cases I and II, the response amplitudes of the stationary wave motions, obtained readily from the evolution equations, compare well with the measurements of Lin & Howard. We also discuss the particular depths at which the third-order asymptotic analyses break down. To obtain uniformly valid descriptions at these particular depths we carry out the perturbation analyses to fifth order and derive the appropriate evolution equations in both cases.

Case III is new and represents the situation when the driving frequency approximates both a natural frequency of the directly forced longitudinal standing wave and twice that of the standing cross-wave. The forced resonant longitudinal and parametrically resonant cross-waves are of the same order of magnitude and the internal interactions between the two orthogonal waves become significant. For a broad range of physical parameters (water depth, wavemaker amplitude, width-to-length ratio and frequency detuning), these interactions are shown to lead to chaotic wave motions. We derive the evolution equations governing the amplitudes of the longitudinal and transverse waves for such three-dimensional interactions in §5.1. In order to account for the two resonances caused by the wavemaker, which are involved at different orders, two long timescales are employed in the perturbation analysis. The equilibrium states (stationary solutions) of the evolution equations and their local stability are discussed in §5.2. Numerical simulations of the evolutions are performed in §5.3, and sample results showing temporal chaotic motions in a number of resonance conditions are presented. The chaotic nature of the evolutions are further confirmed through estimates of the Lyapunov characteristic exponents and power spectra of the amplitudes. In view of the number of physical parameters involved, and to obtain a *global* criterion for the likelihood of widespread chaotic behaviour, we adopt the resonance overlap approximation of Chirikov (1979) to the present problem in §6. This approach is shown to yield remarkably good predictions of the global evolution behaviour of the present system.

In recent years, the generic two-degree-of-freedom internally resonant system of weakly nonlinear gravity waves in a (rectangular or circular) cylinder subject to either horizontal (directly forced) or vertical (parametrically resonant) excitation has been widely studied, primarily for the weakly dissipative system. These include, for example, Keolian *et al.* (1981), Gollub & Meyer (1983), Ciliberto & Gollub (1984, 1985*a, b*), Meron & Procaccia (1986*a, b*, 1987), Nayfeh (1987), Umeki & Kambe (1989) for the vertically oscillated circular cylinder; Gu & Sethna (1987), Feng & Sethna (1989), Simonelli & Gollub (1989) for the vertically oscillated square cylinder; and Miles (1984*b*), Funakoshi & Inoue (1987, 1988) for the horizontally oscillated circular cylinder. As pointed out earlier, the present Cases I and II differ mainly in detail and in providing direct comparisons to the measurements of Lin & Howard (1960). The dynamic system of Case III, however, is new and differs from the above problems in the incorporation of both direct and parametric excitation simultaneously.

We have not considered dissipation in this work, although it is known that such effects play a role in the physical problem (Shemer & Kit 1988). A small, phenomenological linear damping term can be readily included in the evolution equations (e.g. Miles 1984*b*) and much of the present analyses carried out accordingly.

Preliminary results indicate that for weakly dissipative systems Hamiltonian chaos is preserved. Although the method of resonance overlap is strictly applicable only to conservative perturbations, it may be a useful analysis tool for some weakly dissipative problems by providing a global solution to the corresponding Hamiltonian system with the dissipation terms neglected. These and related investigations are currently under way.

2. Formulation of the problem

We consider the fluid motion in a short rectangular wave tank with a wavemaker at rest at $x = 0$, a rigid bottom at $z = -H$, rigid walls at $x = L$ and $y = 0, W$, and a free surface with undisturbed position at $z = 0$. The wavemaker is subject to a harmonic motion given by

$$x = \chi(z,t) = aF(z)\cos\omega_e t, \tag{2.1}$$

where a and ω_e are respectively the amplitude and frequency of the wavemaker motion, and $F(z)$ its shape function normalized by $F(0) = 1$. For a flap-type wavemaker hinged at $z = -d \geqslant -H$, $F(z) = 1 + z/d$ for $0 \geqslant z \geqslant -d$, and $F(z) = 0$ for $-d \geqslant z \geqslant -H$; and for a piston wavemaker, $F(z) = 1$.

In what follows, all physical variables are non-dimensionalized by the length of the tank L, and the timescale $2/\omega_e$. The fluid is assumed to be ideal and surface tension is ignored. For irrotational motion, the velocity potential $\Phi(x,y,z,t)$ and free-surface elevation $\zeta(x,y,t)$ are then governed by the boundary-value problem:

$$\nabla^2\Phi = 0 \quad (\chi < x < 1, 0 < y < 1/l, \ -h < z < \zeta), \tag{2.2a}$$

$$\frac{\partial\zeta}{\partial t} + \nabla\zeta\cdot\nabla\Phi - \frac{\partial\Phi}{\partial z} = 0 \quad (z = \zeta), \tag{2.2b}$$

$$\frac{\partial\Phi}{\partial t} + \tfrac{1}{2}\nabla\Phi\cdot\nabla\Phi + 4N^2\mu\zeta = 0 \quad (z = \zeta), \tag{2.2c}$$

$$\frac{\partial\Phi}{\partial x} = \frac{\partial\chi}{\partial t} + \frac{\partial\chi}{\partial z}\frac{\partial\Phi}{\partial z} \quad (x = \chi = \epsilon F(z)\cos 2t), \tag{2.2d}$$

$$\frac{\partial\Phi}{\partial x} = 0 \quad (x = 1); \qquad \frac{\partial\Phi}{\partial y} = 0 \quad (y = 0, 1/l); \qquad \frac{\partial\Phi}{\partial z} = 0 \quad (z = -h), \tag{2.2e–g}$$

$$\int_0^{1/l}\int_0^1 \zeta(x,y,t)\,\mathrm{d}x\,\mathrm{d}y = 0, \tag{2.2h}$$

where $l = L/W$ is the length-to-width ratio of the tank, and $\epsilon = a/L \ll O(1)$ measures the amplitude of the wave paddle motion. For convenience, N and μ are defined respectively as $N = \Omega_x/\omega_e \approx 1$ and $\mu = (n\pi\tanh n\pi h)^{-1} \equiv \mu_x$ for the problem of longitudinal standing waves only (Case I); and $N = \Omega_y/\omega_e \approx \frac{1}{2}$ and $\mu = (l\pi\tanh l\pi h)^{-1} \equiv \mu_y$ for the (first-mode) cross-wave problem (Case II). Ω_x and Ω_y are the linear natural frequencies of the longitudinal (x) and transverse (y) standing waves, respectively; and n is the mode number of the longitudinal standing wave.

We introduce perturbation expansions for Φ and ζ:

$$\Phi = \sum_{j=1}^{\infty} \epsilon^{j\nu}\Phi_j, \quad \zeta = \sum_{j=1}^{\infty} \epsilon^{j\nu}\zeta_j, \tag{2.3a, b}$$

where the constant $\nu > 0$ provides the ordering depending on the problem to be solved. For the Laplace equation and all of the linear boundary conditions in (2.2), Φ_j and ζ_j satisfy the same form of the equations as Φ and ζ. Expanding the free-surface boundary conditions (2.2*b*, *c*) in Taylor series about $z = 0$ and substituting the perturbation expansions (2.3) for Φ and ζ, we obtain to the first three orders the following results for the free-surface boundary conditions. For the kinematic boundary condition (2.2*b*):

$$\frac{\partial \zeta_j}{\partial t} - \frac{\partial \Phi_j}{\partial z} = F_j \quad (z = 0), \quad j = 1, 2, \ldots, \tag{2.4a}$$

where

$$F_1 = 0, \quad F_2 = -\nabla\zeta_1 \cdot \nabla\Phi_1 + \zeta_1 \frac{\partial^2 \Phi_1}{\partial z^2}, \tag{2.4b, c}$$

$$F_3 = -\nabla\zeta_1 \cdot \nabla\Phi_2 - \nabla\zeta_2 \cdot \nabla\Phi_1 + \zeta_1 \frac{\partial^2 \Phi_2}{\partial z^2} + \zeta_2 \frac{\partial^2 \Phi_1}{\partial z^2} - \zeta_1 \cdot \nabla\zeta_1 \cdot \nabla\left(\frac{\partial \Phi_1}{\partial z}\right) + \tfrac{1}{2}\zeta_1^2 \frac{\partial^3 \Phi_1}{\partial z^3}; \tag{2.4d}$$

and for the dynamic boundary condition (2.2*c*):

$$\frac{\partial \Phi_j}{\partial t} + 4N^2 \mu \zeta_j = G_j \quad (z = 0), \quad j = 1, 2, \ldots, \tag{2.5a}$$

where

$$G_1 = 0, \quad G_2 = -\zeta_1 \frac{\partial^2 \Phi_1}{\partial t\, \partial z} - \tfrac{1}{2}\nabla\Phi_1 \cdot \nabla\Phi_1, \tag{2.5b, c}$$

$$G_3 = -\zeta_1 \frac{\partial^2 \Phi_2}{\partial t\, \partial z} - \zeta_2 \frac{\partial^2 \Phi_1}{\partial t\, \partial z} - \nabla\Phi_1 \cdot \nabla\Phi_2 + \zeta_1 \cdot \nabla\Phi_1 \cdot \nabla\left(\frac{\partial \Phi_1}{\partial z}\right) - \tfrac{1}{2}\zeta_1^2 \frac{\partial^3 \Phi_1}{\partial t\, \partial z^2}. \tag{2.5d}$$

The wavemaker boundary conditions for Φ_j are similarly obtained by expanding (2.2*d*) about $x = 0$ and substituting (2.3*a*) for Φ. The appearance of forcing due to the wavemaker depends on the specific ordering of the problem. For the resonant longitudinal standing wave only case (Case I), the boundary conditions at $x = 0$ at the first two orders are homogeneous:

$$\frac{\partial \Phi_j}{\partial x} = 0 \quad (x = 0), \quad j = 1, 2, \tag{2.6a}$$

and an inhomogeneous forcing term appears only at third order, $O(\epsilon)$, for Φ_3:

$$\frac{\partial \Phi_3}{\partial x} = \frac{\partial \chi}{\partial t} \quad (x = 0). \tag{2.6b}$$

For the resonant cross-wave only case (Case II) and for the three-dimensional motion case (Case III), the wavemaker boundary conditions for Φ_1 and Φ_2 are respectively (2.6*a*) and (2.6*b*). The boundary condition for Φ_3 for these two cases is given by:

$$\frac{\partial \Phi_3}{\partial x} = -\chi \frac{\partial^2 \Phi_1}{\partial x^2} + \frac{\partial \chi}{\partial z} \frac{\partial \Phi_1}{\partial z} \quad (x = 0). \tag{2.6c}$$

3. Synchronous resonantly forced longitudinal standing waves

If the excitation frequency of the wavemaker is approximately equal to a natural frequency of a longitudinal standing wave in the tank (say, the *n*th spatial harmonic mode), but the length-to-width ratio l is not close to an integral multiple of $\frac{1}{4}$ (for moderately deep water), then only the longitudinal wave is resonantly excited by the motion of the wavemaker. The transverse waves are of higher order in amplitude ($O(\epsilon^{\frac{2}{3}})$) compared to the longitudinal standing waves ($O(\epsilon^{\frac{1}{3}})$) and do not interact with the longitudinal wave motion. In this case, the appropriate choice for the long timescale is $\tau = \epsilon^{\frac{2}{3}}t$. We further define the excitation frequency as $N = \Omega_x/\omega_{\mathrm{e}} = 1+\epsilon^{\frac{2}{3}}\lambda_x$, where λ_x is the detuning parameter between the wavemaker frequency and the linear resonance frequency of the longitudinal standing wave.

Processing the boundary-value problem at successive orders, at the leading ($O(\epsilon^{\frac{1}{3}})$) and second ($O(\epsilon^{\frac{2}{3}})$) orders, the boundary conditions at the wavemaker are homogeneous and the velocity potential Φ_1 and Φ_2 and the free-surface elevation ζ_1 and ζ_2 can be solved readily. The aim is to obtain the equation governing the evolution of the complex amplitude envelope $A(\tau)$ of the first-order motion:

$$\Phi_1 = [A(\tau)\,\mathrm{e}^{-\mathrm{i}2t} + \mathrm{c.c.}]\cos n\pi x \frac{\cosh n\pi(z+h)}{n\pi \sinh n\pi h}, \tag{3.1}$$

where c.c. stands for the complex conjugate of the preceding term. At the third order, $O(\epsilon)$, an inhomogeneous wavemaker boundary condition appears:

$$\frac{\partial \Phi_3}{\partial x} = \frac{\partial \chi}{\partial t} = -\mathrm{i}(\mathrm{e}^{-\mathrm{i}2t} - \mathrm{c.c.})\,F(z) \quad (x = 0). \tag{3.2}$$

To remove this inhomogeneous condition from the wall boundary, we decompose the total potential Φ_3 into two parts (Havelock 1929; Ursell, Dean & Yu 1959):

$$\Phi_3 = \phi_3 - \mathrm{i}(\mathrm{e}^{-\mathrm{i}2t} - \mathrm{c.c.})\,\varphi(x,z), \tag{3.3}$$

where $\varphi(x,z)$ satisfies the Laplace equation and homogeneous boundary conditions on the stationary walls and the bottom, and $\partial\varphi/\partial x = F(z)$ on the wavemaker $x = 0$. For a flat-type wavemaker hinged at $z = -h$, such as those in the experiments of Lin & Howard, φ is given by

$$\varphi(x,z) = \frac{8h^2}{\pi^3}\sum_{m=0}^{\infty}\left[\frac{\sin\dfrac{(2m+1)\pi}{2h}z}{(2m+1)^3}\right] + \frac{16h^2}{\pi^3}\sum_{n=1}^{\infty}\sum_{m=0}^{\infty}\left[\frac{\sin\dfrac{(2m+1)\pi}{2h}z}{(2m+1)[(2m+1)^2+4n^2h^2]}\right]\cos n\pi x$$
$$+\frac{4h^2}{\pi^4}\sum_{m=0}^{\infty}\left[\frac{\cos\dfrac{(2m+1)\pi}{h}(z+h)}{(2m+1)^4}\right] + \frac{8h^2}{\pi^4}\sum_{n=1}^{\infty}\sum_{m=0}^{\infty}\left[\frac{\cos\dfrac{(2m+1)\pi}{h}(z+h)}{(2m+1)^2[(2m+1)^2+n^2h^2]}\right]\cos n\pi x.$$

Substituting (3.3) into the third-order free-surface boundary conditions (2.4) and (2.5), and suppressing the secularity for ϕ_3 and ζ_3, we obtain finally the evolution equation for $A(\tau)$:

$$\mu_x \frac{\mathrm{d}A}{\mathrm{d}\tau} + \mathrm{i}2\lambda_x\mu_x A + \tfrac{1}{4}\delta - \mathrm{i}\Gamma_a A^2 A^* = 0, \tag{3.4}$$

where

$$\delta = \frac{8}{n^3\pi^3 h}\tanh\frac{n\pi h}{2}, \quad \Gamma_a = \frac{1}{32\mu_x}(2+3n^2\pi^2\mu_x^2+12n^4\pi^4\mu_x^4-9n^6\pi^6\mu_x^6). \qquad (3.5a, b)$$

The frequency of the longitudinal standing wave is exactly equal to the frequency of the wavemaker motion and its amplitude is a function of that forcing frequency. This is the so-called *non-isochronicity* property for nonlinear oscillators. The amplitude and stability of the stationary responses of (3.4) are readily obtained. The amplitudes of stationary solutions as a function of detuning λ_x are thus similar to those of an undamped Duffing equation with a change from a 'softening-spring' ($\Gamma_a > 0$) to a 'hardening-spring' ($\Gamma_a < 0$) system as the depth h decreases through h^* (Tadjbakhsh & Keller 1960; Fultz 1962).

At $h = h^*, \Gamma_a = 0$, and the perturbation analysis above breaks down. For h near h^*, then, we expand Φ and ζ as perturbation series in powers of $\epsilon^{\frac{1}{5}}$, choose $N = 1+\epsilon^{\frac{4}{5}}\lambda_x$, and process the perturbation analysis to fifth order. Instead of the cubic nonlinear equation (3.4) for A, we obtain at the fifth order, an evolution equation with quintic nonlinearity:

$$\mu_x \frac{\mathrm{d}A}{\mathrm{d}\tau} + \mathrm{i}2\lambda_x \mu_x A + \tfrac{1}{4}\delta - \mathrm{i}\bar{\Gamma}_a A^3 A^{*2} = 0, \tag{3.6a}$$

where

$$\bar{\Gamma}_a = \frac{n^2\pi^2}{128\mu_x}\left[\tfrac{1151}{6} - \tfrac{7509}{8}n^2\pi^2\mu_x^2 + \tfrac{52919}{48}n^4\pi^4\mu_x^4 + \tfrac{14683}{24}n^6\pi^6\mu_x^6 \right.$$
$$\left. - \tfrac{6093}{8}n^8\pi^8\mu_x^8 + 45n^{10}\pi^{10}\mu_x^{10} + \tfrac{2565}{16}n^{12}\pi^{12}\mu_x^{12}\right]. \tag{3.6b}$$

This quintic nonlinear equation is valid for $|h-h^*| \leqslant O(\epsilon^{\frac{2}{5}})$ for $\lambda_x \leqslant O(1)$.

When the natural frequency of an mth spatial harmonic wave becomes an integral multiple of that of the fundamental nth harmonic ($m \neq n$) at certain values of λ, the first-order solution above becomes non-unique (Tadjbakhsh & Keller 1960). Physically, at these depths both the nth and mth spatial harmonics are excited at first order, and there is an internal resonance between the two waves. The coupling interaction of such internal resonance is cubic nonlinear, and the equations governing the evolution of these internal resonant waves can be derived in a similar manner.

Finally, we show comparisons between the present analytic results and Lin & Howard's (1960) experimental measurements. Figure 1 plots the frequency amplitude relation for the stationary resonantly forced longitudinal standing waves. The circles represent the experimental measurements, and the solid and broken lines are stable and unstable stationary solutions respectively of (3.4). The amplitudes of the excitation are given by the maximum deflection, θ, of the wavemaker according to Lin & Howard. Figure 1 (*a*) is for tank dimension $L = 18$ in., $H = 24$ in. and $2\theta = 0.566°$, and the resonant motion is the first-mode ($n = 1$) standing wave. The comparisons between the theoretical and experimental results are remarkably good for the entire range of detuning frequency. Figure 1 (*b*) is for the case $L = 29.5$ in., $H = 24$ in., $2\theta = 0.935°$, and the resonant standing wave is the second mode ($n = 2$). The comparisons are fairly good except for large detuning values where the total response is small and other modes may have begun to participate. For the present case, Lin & Howard (1960) also obtained theoretical results using a direct perturbation expansion similar to that of Penney & Price (1952). The resulting analysis was fairly involved and they were only able to obtain results for the first-mode ($n = 1$) resonance and for deep water. Because of this, and possibly also due to algebraic errors, their comparison to the $n = 1$ case (figure 1*a*) was not as satisfactory.

4. Subharmonic parametrically resonant transverse standing waves

When the wavemaker excitation is close to twice the frequency of a cross-tank standing wave but the length of the tank is such that the longitudinal standing wave is not resonant, the former is resonantly excited and the latter is of higher order in amplitude. Following the experiments and analysis of Lin & Howard (1960) for the problem, Garrett (1970) showed that the mechanism for cross-wave excitation is

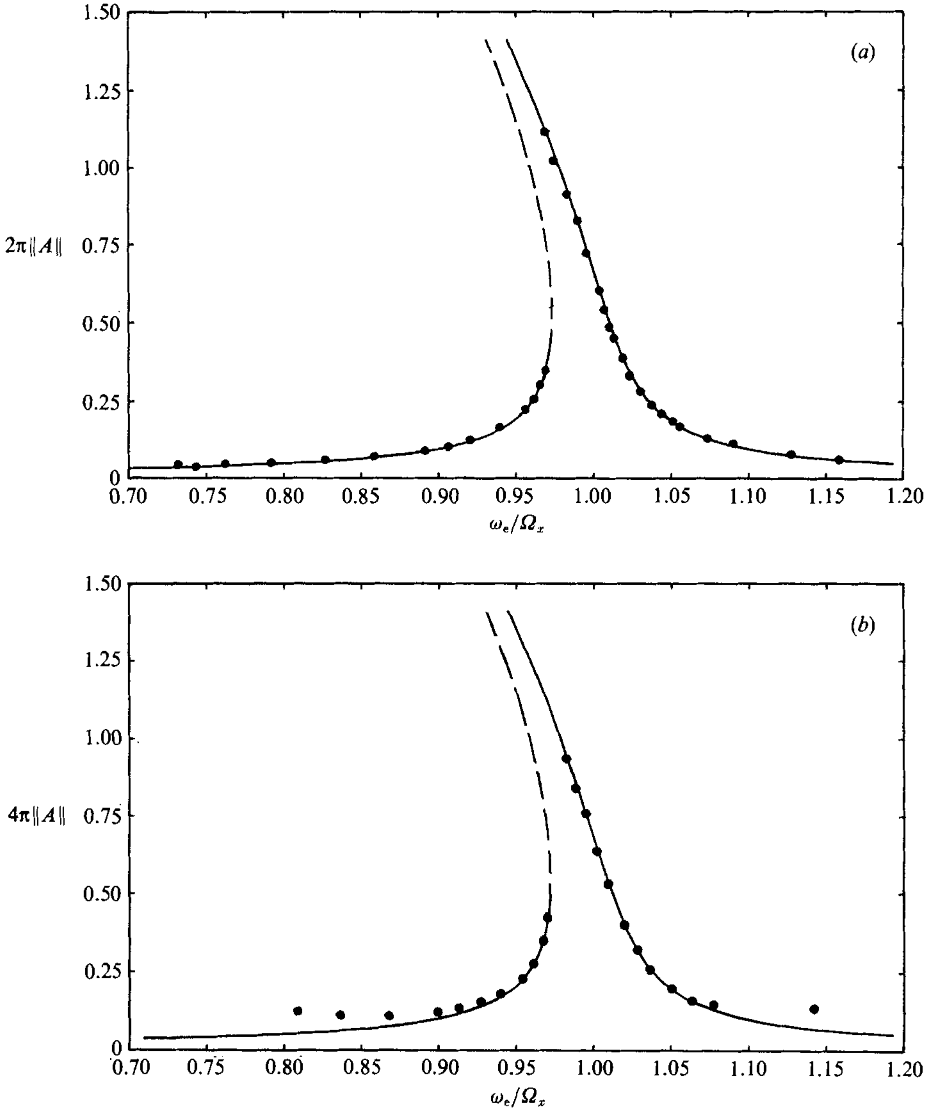

FIGURE 1. Comparisons of the frequency–response relationship for stationary longitudinal waves between the present analytic results (solid lines for stable and broken lines for unstable responses) and Lin & Howard's (1960) experimental measurements (circles) for (*a*) $n = 1$, $L = 18$ in., $h = 24$ in., $2\theta = 0.566°$; and (*b*) $n = 2$, $L = 29.5$ in., $H = 24$ in., $2\theta = 0.935°$.

indeed one of parametric resonance characterized by forcing terms which appear as coefficients of the differential equation.

For this problem, we consider the $\frac{1}{2}$ subharmonic parametric-resonant cross-waves, choose the long timescale $\tau = \epsilon t$ and define the transverse detuning λ_y as $N = \Omega_y/\omega_e = \frac{1}{2}+\epsilon\lambda_y$. The length-to-width ratio l is assumed to be far from integral multiples of $\frac{1}{4}$ so that the longitudinal wave is not resonantly excited. Since the longitudinal wave is of higher order, at leading order, $O(\epsilon^{\frac{1}{2}})$, the velocity potential Φ_1 is independent of x:

$$\Phi_1 = \tfrac{1}{2}[B(\tau)\,e^{-it} + \text{c.c.}] \cos l\pi y \frac{\cosh l\pi(z+h)}{l\pi \sinh l\pi h}, \tag{4.1}$$

where $B(\tau)$ is the complex amplitude envelope of the cross-wave. At the next order, Φ_2 satisfies the inhomogeneous wavemaker boundary condition (3.2) at $x = 0$. The same procedure as (3.3) is applied and the second order Φ_2 and ζ_2 can be solved accordingly. Note that there is a mean set-up of $\frac{1}{4}h(\mathrm{e}^{-\mathrm{i}2t} + \mathrm{c.c.})$ in the second-order free-surface elevation which is equal to the fluid volume displaced by the wavemaker, $\int_{-h}^{0} \xi(z,t)\,\mathrm{d}z$. This mean free-surface elevation is the only contribution from the wavemaker at this order ($O(\epsilon)$) which causes a secularity at the next order ($O(\epsilon^{\frac{3}{2}})$) through its interaction with the transverse wave.

At third order, $O(\epsilon^{\frac{3}{2}})$, the inhomogeneous wavemaker boundary condition is

$$\frac{\partial \Phi_3}{\partial x} = \frac{\partial \chi}{\partial z}\frac{\partial \Phi_1}{\partial z} \quad (x = 0). \tag{4.2}$$

From (4.2), we see that the resonant excitation of the cross-wave is caused directly by the interaction between the wavemaker motion and the transverse wave without involving the longitudinal waves. Again, we transform the inhomogeneous boundary condition by the substitution

$$\Phi_3 = \phi_3 + (B^* \mathrm{e}^{-\mathrm{i}t} + B\,\mathrm{e}^{-\mathrm{i}3t} + \mathrm{c.c.})\,\theta(x,z)\cos l\pi y, \tag{4.3a}$$

where

$$\theta(x,z) = \frac{\cosh l\pi h - 1}{l\pi^4 h^2 \sinh l\pi h} \sum_{m=0}^{\infty} \left[\frac{\sin m_1 \pi z}{2m+1}\left(\frac{1}{l^2+m_1^2} + \frac{2}{\pi}\sum_{n=1}^{\infty} \frac{\cos n\pi x}{l^2+m_1^2+n^2}\right)\right]$$
$$- \frac{l}{2\pi^3 h^2 \sinh l\pi h} \sum_{m=0}^{\infty} \left[\frac{[(-1)^m \cosh l\pi h - 1]\cos m_2 \pi(z+h)}{l^2+m_2^2}\left(\frac{1}{l^2+m_2^2} + \frac{2}{\pi}\sum_{n=1}^{\infty} \frac{\cos n\pi x}{l^2+m_2^2+n^2}\right)\right], \tag{4.3b}$$

and $m_1 = (2m+1)/2h$, $m_2 = m/h$. Combining the kinematic and dynamic free-surface boundary conditions for ϕ_3 and applying the solvability condition yields the evolution equation for $B(\tau)$:

$$\mu_y \frac{\mathrm{d}B}{\mathrm{d}\tau} + \mathrm{i}2\lambda_y \mu_y B - \mathrm{i}\beta B^* - \mathrm{i}\Gamma_b B^2 B^* = 0, \tag{4.4}$$

where

$$\beta = \frac{1}{\mu_y}(1 + l^2\pi^2\mu_y^2)(f_0 - d_0) - \tfrac{1}{2}f_0' + \tfrac{1}{2}\mu_y f_0'' + \tfrac{1}{4}g_0 - \tfrac{1}{4}\mu_y g_0', \tag{4.5a}$$

$$\Gamma_b = \frac{1}{64\mu_y}(2 + 3\mu_y^2 l^2\pi^2 + 12\mu_y^4 l^4\pi^4 - 9\mu_y^6 l^6\pi^6), \tag{4.5b}$$

$$f_0 = -\tfrac{1}{24}h^2, \quad f_0' = \tfrac{1}{2}h, \quad f_0'' = 1, \tag{4.5c}$$

$$g_0 = -\frac{1}{2l^2\pi^2 h} + \frac{1}{l^3\pi^3 h^2}\tanh \tfrac{1}{2}l\pi h, \quad g_0' = \frac{1}{l^2\pi^2 h^2}\tanh l\pi h \tanh \tfrac{1}{2}l\pi h. \tag{4.5d}$$

The coefficient β of B^* in (4.4) represents the parametric resonance and is negative for all depths. Note that the f-terms in β come from the first-order wavemaker boundary condition, and are equivalent to those of Garrett's linear results obtained by averaging the longitudinal motions. The g-terms in β correspond to the second-order wavemaker boundary condition representing the direct interaction between the motions of the wavemaker and the cross-wave. The primes on f and g denote respectively derivatives with respect to z of $\varphi(x,z)$ and $\theta(x,z)$; and the zero subscripts

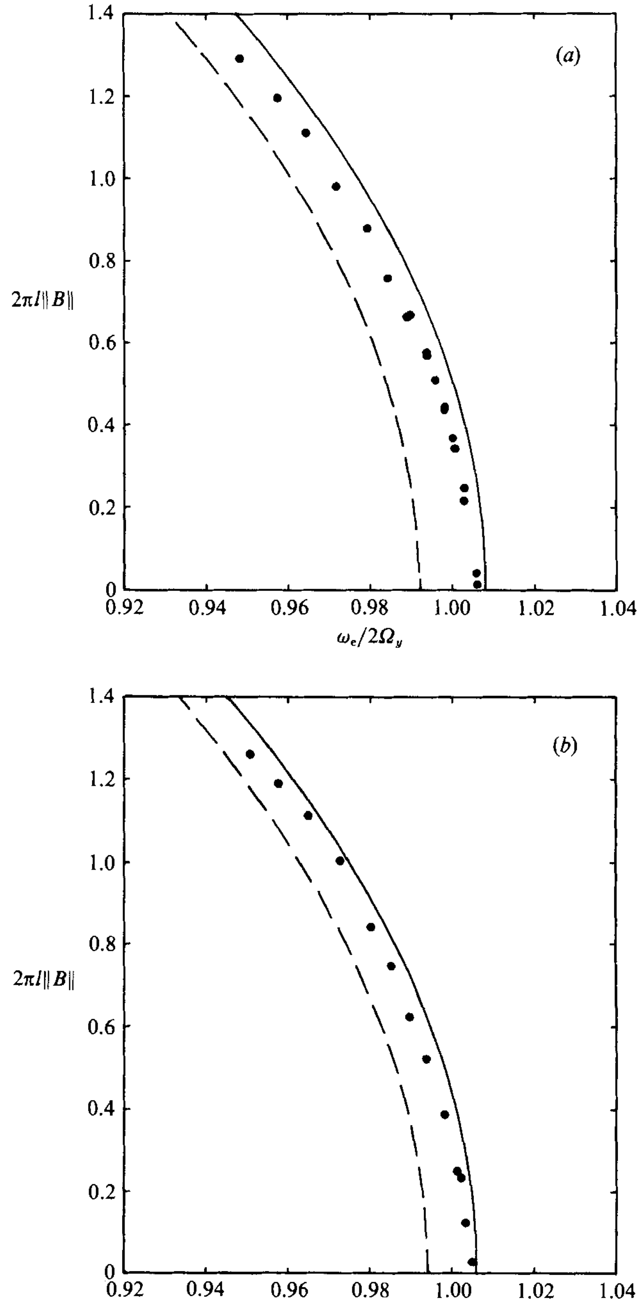

FIGURE 2. Comparisons of the frequency–response relationship for stationary cross-waves between the present results (solid lines for stable and broken lines for unstable responses) and Lin & Howard's (1960) experimental measurements (circles) for $H = 24$ in., $W = 24.1875$ in. and (*a*) $L = 7$ in., $2\theta = 0.287°$; and (*b*) $L = 8.75$ in., $2\theta = 0.279°$.

mean that only the constant terms in the series contribute to resonance. For example, g_0' is the contribution coming from the constant terms of $\partial\varphi/\partial z$ at $z = 0$.

Equation (4.4) is isomorphic to equation (4.1) of Miles (1984*a*) and equation (5.1) of Miles (1988) after a $\frac{1}{4}\pi$ phase shift of his complex amplitude. The details of the phase-plane trajectories and stability analysis of the stationary solutions of (4.4) can be found in Miles (1984*a*). For the stable response, the free surface is flat when the wavemaker reaches its outermost position; while for the unstable response the free surface is flat when the wavemaker is in its innermost position. This phase relation was also observed in Lin & Howard's experiments. Note that since β is negative in the whole range of water depth, the phase-plane trajectories of (4.4) correspond to a $\frac{1}{2}\pi$ rotation of those in figure 2 of Miles (1984*a*). For *periodic* solutions, the evolution equation (4.4) can be integrated in closed form in terms of elliptic integrals (e.g. Struble 1963; Tsai & Yue 1988).

Again, we note that there exists a depth $h = h^{**}$ where $\Gamma_b(h^{**}) = 0$, and the perturbation analysis above breaks down. To obtain a uniformly valid description near that depth, we expand Φ and ζ in powers of $\epsilon^{\frac{1}{4}}$, and carry out the perturbation to $O(\epsilon^{\frac{5}{4}})$. The final evolution equation is

$$\mu_y \frac{\mathrm{d}B}{\mathrm{d}z} + \mathrm{i}2\lambda_y \mu_y B - \mathrm{i}\beta B^* - \mathrm{i}\bar{\Gamma}_b B^3 B^{*2} = 0, \tag{4.6a}$$

where

$$\bar{\Gamma}_b = \frac{l^2\pi^2}{1024\mu_y}\left[\tfrac{1151}{6} - \tfrac{7509}{8} l^2\pi^2\mu_y^2 + \tfrac{52919}{48} l^4\pi^4\mu_y^4 + \tfrac{14683}{24} l^6\pi^6\mu_y^6 - \tfrac{6093}{8} l^8\pi^8\mu_y^8 + 45 l^{10}\pi^{10}\mu_y^{10} \tfrac{2526}{16} l^{12}\pi^{12}\mu_y^{12}\right]. \tag{4.6b}$$

Finally, we compare the present results to the measurements of Lin & Howard (1960). Figure 2 shows these comparisons for the frequency–amplitude relation of the stationary resonant cross-waves. The dimensional parameters are $L = 7$ in., $2\theta = 0.287°$ (figure 2*a*) and $L = 8.75$ in., $2\theta = 0.279°$ (figure 2*b*) respectively, with $H = 24$ in., $W = 24.1875$ in. in both cases. The present results are in reasonably good agreement with the experimental data but with a slight overprediction of the response amplitudes which may be due to the absence of dissipation in the present theoretical model.

5. Interaction between resonant longitudinal and transverse standing waves

5.1. *Evolution equations*

When the excitation frequency of the wavemaker is approximately equal to the natural frequency of the longitudinal *n*th harmonic standing wave and the length-to-width ratio l is close to $\frac{1}{4}n$ (for first-mode cross-waves), the longitudinal wave is directly resonated by the wavemaker while the transverse wave is parametrically excited. Both waves are now of the same order of magnitude, $O(\epsilon^{\frac{1}{2}})$, and internal interactions must be included. To account for the two resonances which are involved at different orders, two long timescales are introduced: $\tau_1 = \epsilon^{\frac{1}{2}}t$ and $\tau_2 = \epsilon t$. The relative degrees of resonance between the wavemaker motion and the longitudinal and transverse standing waves are measured by $\Omega_y/\omega_{\mathrm{e}} = \frac{1}{2} + \epsilon^{\frac{1}{2}}\lambda$ and $\Omega_x/\Omega_y = 2 + \epsilon^{\frac{1}{2}}\gamma$, where λ and γ are the detuning parameters.

The first-order velocity potential for this case of three-dimensional wave motion is

$$\Phi_1 = [A(\tau_1, \tau_2)\,\mathrm{e}^{-\mathrm{i}(2+\gamma\epsilon)t} + \mathrm{c.c.}]\cos n\pi x \frac{\cosh n\pi(z+h)}{n\pi \sinh h\pi h} + \tfrac{1}{2}[B(\tau_1, \tau_2)\,\mathrm{e}^{-\mathrm{i}t} + \mathrm{c.c.}]\cos n\pi y \frac{\cosh l\pi(z+h)}{l\pi \sinh l\pi h}. \tag{5.1}$$

At the second order, $O(\epsilon)$, the inhomogeneous wavemaker boundary condition (3.2) results in a secular forcing which gives the following solvability condition for Φ_2:

$$\mu\frac{\partial A}{\partial \tau_1}+\mathrm{i}2\lambda\mu(2+\gamma\epsilon^{\frac{1}{2}})\,A+(1+\gamma\epsilon^{\frac{1}{2}})\,\delta\,\mathrm{e}^{\mathrm{i}\gamma\tau_1}=0, \tag{5.2a}$$

and

$$\mu\frac{\partial B}{\partial \tau_1}+\mathrm{i}2\lambda\mu B=0, \tag{5.2b}$$

where $\mu\equiv\mu_y\approx 4\mu_x$ and δ is given in (3.5a). The higher-order terms in the coefficients of (5.2a) come from expressing μ_x and μ_y in terms of the common μ and are retained to be consistent at the next order. Note that because of the detuning between the natural frequencies of the longitudinal and cross-waves, $\mu_y/\mu_x=(\Omega_x/\Omega_y)^2=4+O(\epsilon^{\frac{1}{2}})$, the corresponding error in the evolution equation at third order will be $O(\epsilon^{\frac{1}{2}})$ if we replace μ_x by $\frac{1}{4}\mu_y$ in the sequel. Applying (5.2a) and (5.2b) to the second-order boundary-value problem, we can solve for Φ_2 and ζ_2 (see the Appendix).

At third order, $O(\epsilon^{\frac{3}{2}})$, the inhomogeneous wavemaker boundary condition (2.6c) appears. Since the first term of the forcing in (2.6c) does not cause resonant secularity, only the form of the boundary condition (4.2) needs to be considered and the same substitution as (4.3a) is used for Φ_3. Combining the free-surface boundary conditions, sorting out the secular forcing terms and invoking the solvability condition for ϕ_3, we obtain the evolution equations with modulation timescale τ_2:

$$\mu\frac{\partial A}{\partial \tau_2}+\mathrm{i}4\lambda^2\mu A+\lambda\delta\,\mathrm{e}^{\mathrm{i}\gamma\tau_1}-\mathrm{i}\Gamma_a A^2A^*-\mathrm{i}\Sigma_a ABB^*=0, \tag{5.3a}$$

and

$$\mu\frac{\partial B}{\partial \tau_2}+\mathrm{i}2\lambda^2\mu B-\mathrm{i}\beta B^*-\mathrm{i}\Gamma_b B^2B^*-\mathrm{i}\Sigma_b BAA^*=0, \tag{5.3b}$$

where δ is given by (3.5a), β by (4.5a), Γ_a is four times the expression (3.5b), and Γ_b is the same as (4.5b). The coefficients Σ_a and Σ_b governing the nonlinear coupling between the longitudinal and transverse waves are given by

$$\Sigma_a=a_2[1-\tfrac{1}{2}(\tfrac{1}{2}n^2+l^2)\,\pi^2\mu\tilde{\mu}]+b_2[-1+\tfrac{1}{2}(\tfrac{1}{2}n^2-l^2)\,\pi^2\mu\tilde{\mu}]+\tfrac{1}{2}\tilde{a}_2-\tfrac{1}{2}\tilde{b}_2-\tfrac{1}{4}\pi^2l^2\mu, \tag{5.4a}$$

$$\Sigma_b=\tfrac{1}{2}\Sigma_a. \tag{5.4b}$$

Equations (5.2) and (5.3) respectively govern the evolution of the first-order amplitudes with respect to τ_1 and τ_2, and A and B in general vary over both τ_1 and τ_2 (see figure 7 for some sample evolutions). Since τ_1 appears explicitly in (5.3a), it is more convenient to consider A and B as functions of τ_1 (only), and combine (5.2a, b) and (5.3a, b) into a single pair of equations. Defining $\tau_1\equiv\tau$ for convenience, recalling the chain rule $(\partial/\partial\tau_1)+\epsilon^{\frac{1}{2}}(\partial/\partial\tau_2)\rightarrow(\partial/\partial\tau)$, and factoring out the modulation of the forcing in (5.2a) and (5.3a) by letting $A\equiv\sqrt{2}\tilde{A}\,\mathrm{e}^{\mathrm{i}\gamma\epsilon\tau}$, we obtain the final result

$$\mu\frac{\mathrm{d}\tilde{A}}{\mathrm{d}\tau}+\mathrm{i}\gamma_a\tilde{A}+\tilde{\delta}-\mathrm{i}\tilde{\Gamma}_a\tilde{A}^2\tilde{A}^*-\mathrm{i}\tilde{\Sigma}_a\tilde{A}BB^*=0 \tag{5.5a}$$

and

$$\mu\frac{\mathrm{d}B}{\mathrm{d}\tau}+\mathrm{i}\gamma_b B-\mathrm{i}\tilde{\beta}B^*-\mathrm{i}\tilde{\Gamma}_b B^2B^*-\mathrm{i}\tilde{\Sigma}_b B\tilde{A}\tilde{A}^*=0, \tag{5.5b}$$

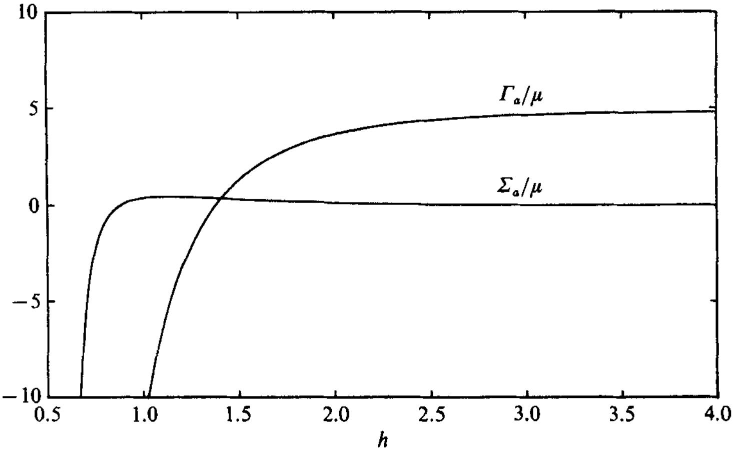

FIGURE 3. Parameters Γ_a/μ and Σ_a/μ plotted against water depth h for $n = 1$ and $l = 0.248062$.

where

$$\gamma_a = \mu[4\lambda+\gamma+2\epsilon^{\frac{1}{2}}(\lambda\gamma+2\lambda^2)], \quad \gamma_b = 2\mu[\lambda+\epsilon^{\frac{1}{2}}\lambda^2], \tag{5.6a, b}$$

$$\tilde{\delta} = \frac{\delta}{\sqrt{2}}[1+\epsilon^{\frac{1}{2}}(\gamma+\lambda)], \quad \tilde{\beta} = \epsilon^{\frac{1}{2}}\beta, \quad \tilde{\Gamma}_a = 2\epsilon^{\frac{1}{2}}\Gamma_a, \quad \tilde{\Gamma}_b = \epsilon^{\frac{1}{2}}\Gamma_b, \tag{5.6c–f}$$

$$\tilde{\Sigma}_a = \epsilon^{\frac{1}{2}}\Sigma_a = 2\epsilon^{\frac{1}{2}}\Sigma_b = \tilde{\Sigma}_b \equiv \tilde{\Sigma}. \tag{5.6g}$$

The evolution equation (5.5*a*) reduces to (3.4) for the longitudinal wave amplitude in the absence of the transverse wave, and the transverse wave equation (5.5*b*) reduces to (4.4) if the longitudinal motions are small.

If we write $\tilde{A} \equiv C_a + \mathrm{i}D_a$ and $B \equiv C_b + \mathrm{i}D_b$, (5.5*a*, *b*) can be represented as an autonomous Hamiltonian system with the Hamiltonian $\mathscr{H}$ given by

$$\begin{aligned}\mathscr{H} = -\frac{1}{\mu}[&\tilde{\delta}D_a + \tfrac{1}{2}\tilde{\beta}(C_b^2-D_b^2) - \tfrac{1}{2}\gamma_a(C_a^2+D_a^2) + \tfrac{1}{4}\tilde{\Gamma}_a(C_a^2+D_a^2)^2 \\ &-\tfrac{1}{2}\gamma_b(C_b^2+D_b^2) + \tfrac{1}{4}\tilde{\Gamma}_b(C_b^2+D_b^2)^2 + \tfrac{1}{2}\tilde{\Sigma}(C_a^2+D_a^2)(C_b^2+D_b^2)].\end{aligned} \tag{5.7}$$

The conjugate variables C_a, D_a and C_b, D_b satisfy the Hamiltonian equations

$$\frac{\mathrm{d}C_{a,b}}{\mathrm{d}\tau} = \frac{\partial \mathscr{H}}{\partial D_{a,b}}, \quad \frac{\mathrm{d}D_{a,b}}{\mathrm{d}\tau} = -\frac{\partial \mathscr{H}}{\partial C_{a,b}}. \tag{5.8a, b}$$

The Hamiltonian system (5.8) is invariant under the reflection $(C_b, D_b) \rightarrow -(C_b, D_b)$ by virtue of symmetry with respect to the centreplane of the wave tank $y = \frac{1}{2}W$.

The coefficients $\Gamma_{a,b}$ and $\Sigma_{a,b}$ of the cubic nonlinear terms in the evolution equations, which govern the self- and internal interactions respectively, are functions of the length-to-width ratio l, longitudinal wavenumber n, and water depth h. Figure 3 shows Γ_a/μ and Σ_a/μ as the functions of h for $n = 1$ and $l = 6.0/24.1875 \approx 0.248062$ (a value corresponding to that of RUN 101 in Lin & Howard's experiment). For shallow depths, the magnitudes of Γ_a and Σ_a become much larger than $O(1)$ and the present perturbation analysis becomes invalid. For deep water, Γ_a is $O(1)$ while Σ_a approaches a small value, and the interaction between the longitudinal and cross-waves becomes weak. The internal interaction is strongest around intermediate depths, where the magnitudes of Γ_a and Σ_a are comparable. For higher n with the corresponding l, the coefficients of the nonlinear terms have behaviour similar to that for the $n = 1$ mode.

5.2. *Stationary solutions and bifurcation diagrams*

The stationary solutions of the evolution equations (5.8*a*, *b*) are given by

$$\left.\begin{aligned} C_{a0} = 0, \quad C_{b0} = 0, \quad D_{b0} = 0, \\ \tilde{\Gamma}_a D_{a0}^3 - \gamma_a D_{a0} + \tilde{\delta} = 0, \end{aligned}\right\} \tag{5.9a}$$

$$\left.\begin{aligned} & C_{a0} = 0, \quad D_{b0} = 0, \\ & D_{a0}^3 + \frac{[\tilde{\Gamma}_b \gamma_a - \tilde{\Sigma}_a(\gamma_b - \tilde{\beta})]}{\Xi_{ab}} D_{a0} - \frac{\tilde{\delta}\tilde{\Gamma}_b}{\Xi_{ab}} = 0, \\ & C_{b0} = \pm\left[\frac{(\gamma_b - \tilde{\beta}) - \tilde{\Sigma}_b D_{a0}^2}{\tilde{\Gamma}_b}\right]^{\frac{1}{2}}, \end{aligned}\right\} \tag{5.9b}$$

$$\left.\begin{aligned} & C_{a0} = 0, \quad C_{b0} = 0, \\ & D_{a0}^3 + \frac{[\tilde{\Gamma}_b \gamma_a - \tilde{\Sigma}_a(\gamma_b + \tilde{\beta})]}{\Xi_{ab}} D_{a0} - \frac{\tilde{\delta}\tilde{\Gamma}_b}{\Xi_{ab}} = 0, \\ & D_{b0} = \pm\left[\frac{(\gamma_b + \tilde{\beta}) - \tilde{\Sigma}_b D_{a0}^2}{\tilde{\Gamma}_b}\right]^{\frac{1}{2}}, \end{aligned}\right\} \tag{5.9c}$$

where $\Xi_{ab} \equiv \tilde{\Sigma}_a \tilde{\Sigma}_b - \tilde{\Gamma}_a \tilde{\Gamma}_b$. The solutions (5.9*a*) correspond to the two-dimensional longitudinal waves of §3, while (5.9*b*, *c*) are the stationary three-dimensional wave solutions arising from the coupling between the forced longitudinal wave and the parametrically excited transverse wave.

The stability of these stationary solutions is determined by the real parts of all the eigenvalues ω of the equation

$$F(\omega) = \|\boldsymbol{M}(X = X_0) - \mu\omega \boldsymbol{I}\| = 0, \tag{5.10}$$

where $X \equiv (C_a, D_a, C_b, D_b)$, $\boldsymbol{M} \equiv \partial S/\partial X$, $S \equiv \nabla_X \mathscr{H}$, and $\boldsymbol{I}$ is the unit matrix. One property of (5.10) is that if ω is an eigenvalue, so is $-\omega$. Therefore a stationary solution is stable if, and only if, the eigenvalue ω is pure imaginary.

For the two-dimensional solution (5.9*a*), the eigenvalue equation (5.10) can be simplified as

$$F(\omega) = [\mu^2\omega^2 + (3\tilde{\Gamma}_a D_{a0}^4 - 4\gamma_a \tilde{\Gamma}_a D_{a0}^2 + \gamma_a^2)][\mu^2\omega^2 + (\tilde{\Sigma}_b D_{a0}^4 - 2\gamma_b \tilde{\Sigma}_b D_{a0}^2 + \gamma_b^2 - \tilde{\beta}^2)] = 0. \tag{5.11}$$

The stationary solution is stable if, and only if, $(3\tilde{\Gamma}_a D_{a0}^4 - 4\gamma_a \tilde{\Gamma}_a D_{a0}^2 + \gamma_a^2) > 0$ and $(\tilde{\Sigma}_b D_{a0}^4 - 2\gamma_b \Sigma_b D_{a0}^2 + \gamma_b^2 - \tilde{\beta}^2) > 0$. The first condition determines the stability of the stationary longitudinal wave subject to perturbations in the longitudinal direction. This type of bifurcation corresponds to the turning point. The second inequality refers to the stability of the stationary longitudinal wave subject to transverse perturbations. This is the so-called pitchfork bifurcation which determines the incidence of three-dimensional wave motions. The bifurcation of the two-dimensional transverse wave in §4 is a special case of this kind of bifurcation which bifurcates from the state $D_{a0} = 0$.

For the three-dimensional stationary waves (5.9*b*) and (5.9*c*), (5.10) becomes

$$F(\omega) = \mu^4\omega^4 + F_2\mu^2\omega^2 + F_0 = 0, \tag{5.12}$$

where
$$\begin{aligned} F_2 = {} & D^4_{a0}(\tilde{\Sigma}^2_b + 3\tilde{\Gamma}^2_a) + \left(\frac{C^4_{b0}}{D^4_{b0}}\right)(\tilde{\Sigma}^2_a + 3\tilde{\Gamma}^2_b) + \left(\frac{C^2_{b0}}{D^2_{b0}}\right) D^2_{a0}(4\tilde{\Gamma}_b\tilde{\Sigma}_b + 4\tilde{\Gamma}_a\tilde{\Sigma}_a) \\ & + D^2_{a0}(-2\gamma_b\tilde{\Sigma}_b - 4\gamma_a\tilde{\Gamma}_a) + \left(\frac{C^2_{b0}}{D^2_{b0}}\right)[-2\gamma_a\tilde{\Sigma}_a - (4\gamma_b \pm 2\tilde{\beta})\tilde{\Gamma}_b] \\ & + \gamma^2_a + \gamma^2_b - \tilde{\beta}^2, \end{aligned} \tag{5.13a}$$

and
$$\begin{aligned} F_0 = {} & \pm 2\tilde{\beta}(\tilde{\Gamma}_a D^2_{a0} + \tilde{\Sigma}_a C^2_{b0} - \gamma_a)\Big\{-\gamma_a(\gamma_b \mp \tilde{\beta}) \\ & + D^4_{a0}(-3\tilde{\Gamma}_a\tilde{\Sigma}_b) + \left(\frac{C^4_{b0}}{D^4_{b0}}\right)(-3\tilde{\Gamma}_b\tilde{\Sigma}_a) + \left(\frac{C^2_{b0}}{D^2_{b0}}\right) D^2_{a0}(3\tilde{\Sigma}_a\tilde{\Sigma}_b - 9\tilde{\Gamma}_a\tilde{\Gamma}_b) \\ & + D^2_{a0}[\gamma_a\tilde{\Sigma}_b + (3\gamma_b \mp 3\tilde{\beta})\tilde{\Gamma}_a] + \left(\frac{C^2_{b0}}{D^2_{b0}}\right)[(\gamma_b \mp \tilde{\beta})\tilde{\Sigma}_a + 3\gamma_a\tilde{\Gamma}_b]\Big\}. \end{aligned} \tag{5.13b}$$

The upper and lower expressions in (5.13*a*) and (5.13*b*) correspond to the stationary solutions (5.9*b*) and (5.9*c*), respectively. The necessary and sufficient conditions for (5.12) to have pure imaginary solutions ω, i.e. for the critical points to be stable, are $F_2 > 0, F_0 > 0$ and $F^2_2 - 4F_0 > 0$.

The system (5.8) has a total of five parameters: h, l, λ, ϵ and n. For a given tank dimension and wavemaker amplitude, h, l, ϵ and n are constant. We thus perform the bifurcation analysis of codimension-one in terms of the detuning λ of the excitation frequency. Figure 4 shows the bifurcation diagram of the amplitude of the stationary solution, $[(C^2_{a0} + D^2_{a0}) + 0.5(C^2_{b0} + D^2_{b0})]^{\frac{1}{2}}$, as a function of the detuning parameter λ, for $l = 0.248062$, $n = 1$, $\epsilon = 0.009072$ and different water depths, $h = 1.5$, 1.6, 1.7, 1.9, 2.2, 4.0. The solid and broken lines in the figures represent respectively the stable centres and unstable saddle points of the stationary solutions. The branches labelled (*a*), (*b*), and (*c*) correspond to the families (5.9*a*), (5.9*b*) and (5.9*c*) respectively.

The features of the bifurcation diagrams change abruptly around the intermediate depths, $h = 1.5$–1.9. For h greater than 2.5, the bifurcation diagrams are qualitatively similar to that of the $h = 4.0$ case. For $h = 1.5$ and 1.6, a three-dimensional wave family, branch (b_3), bifurcates from the family of two-dimensional longitudinal waves (a_3). Along this three-dimensional family, both longitudinal and transverse components grow with increasing detuning λ, but the transverse wave increases at a faster rate. Stability of this three-dimensional wave is lost when the transverse wave grows to about one order of magnitude greater than the longitudinal wave, and the wave motion becomes essentially that of a two-dimensional cross-wave.

Figure 5 shows the real and imaginary parts of the eigenvalue ω along the branch (b_3) for $h = 1.6$. The branch starts at the pitchfork bifurcation point $\lambda = \lambda_1$ where a pair of pure imaginary eigenvalues separate into two pairs along the imaginary ω-axis. These two pairs of ω coalesce in pairs again along the imaginary axis at $\lambda = \lambda_2$ and then split into two complex-conjugate pairs leaving the imaginary axis. This kind of bifurcation at $\lambda = \lambda_2$ is known as Hamiltonian–Hopf bifurcation. It corresponds to the Benjamin–Feir instability (Benjamin & Feir 1967) for two-dimensional steady progressive waves (Zufiria 1988). Continuing along the branch (b_3), the two pairs of conjugate-complex eigenvalues coalesce on the real ω-axis at $\lambda = \lambda_3$, and then split into another two pairs of real eigenvalues along the real ω-axis. It should be mentioned that at the bifurcation point $\lambda = \lambda_2$, where the three-

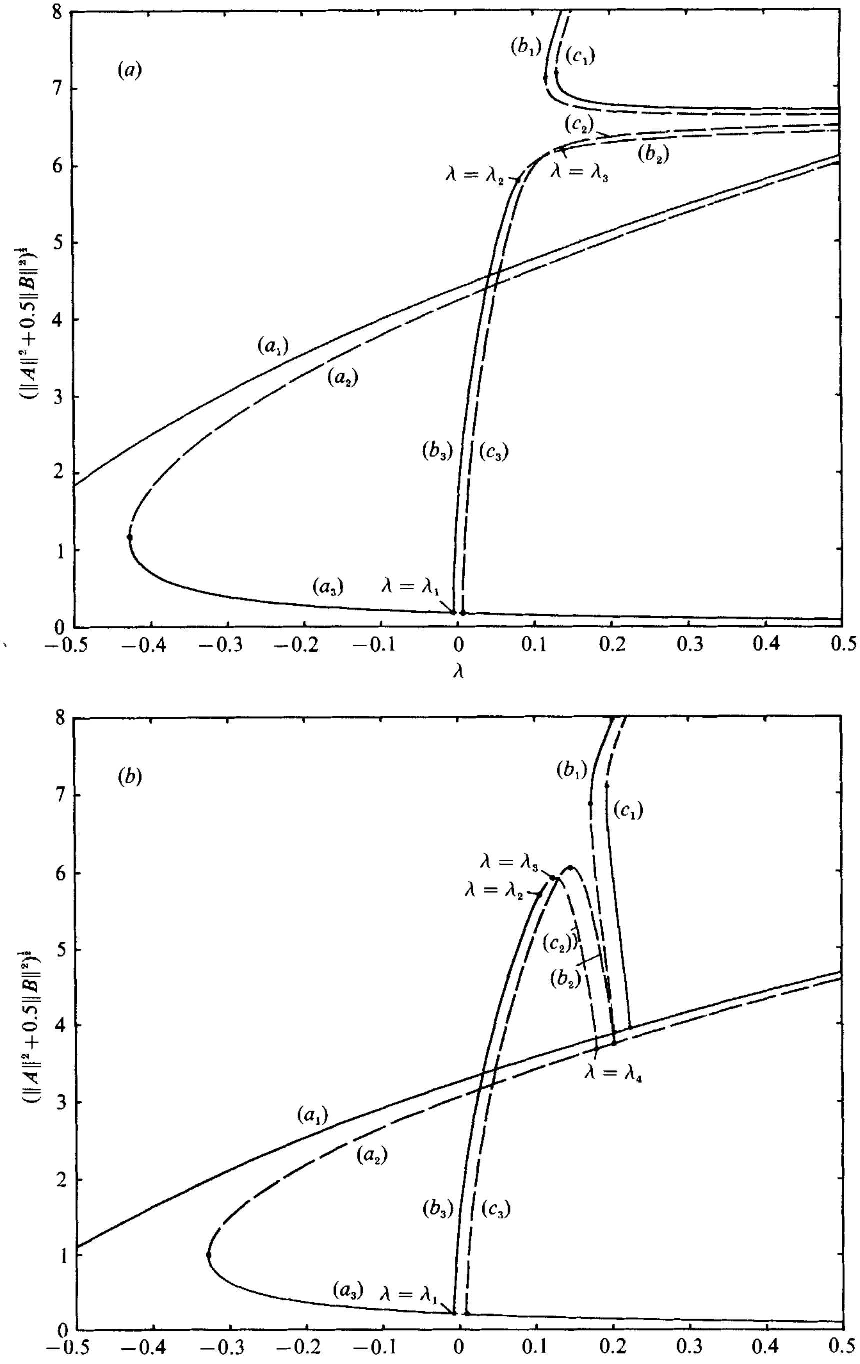

FIGURE 4(*a*,*b*). For caption see p. 360.

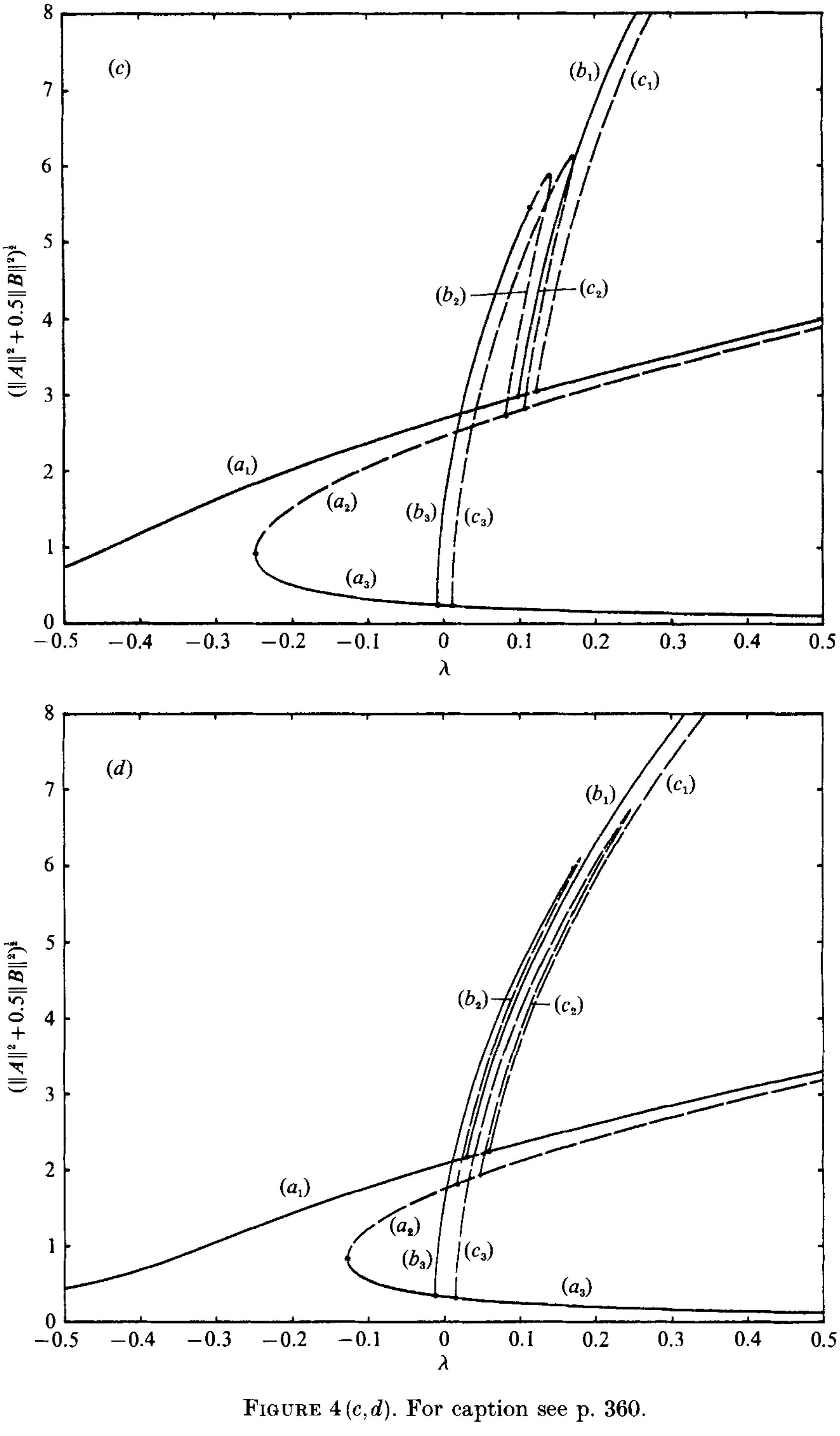

FIGURE 4 (c, d). For caption see p. 360.

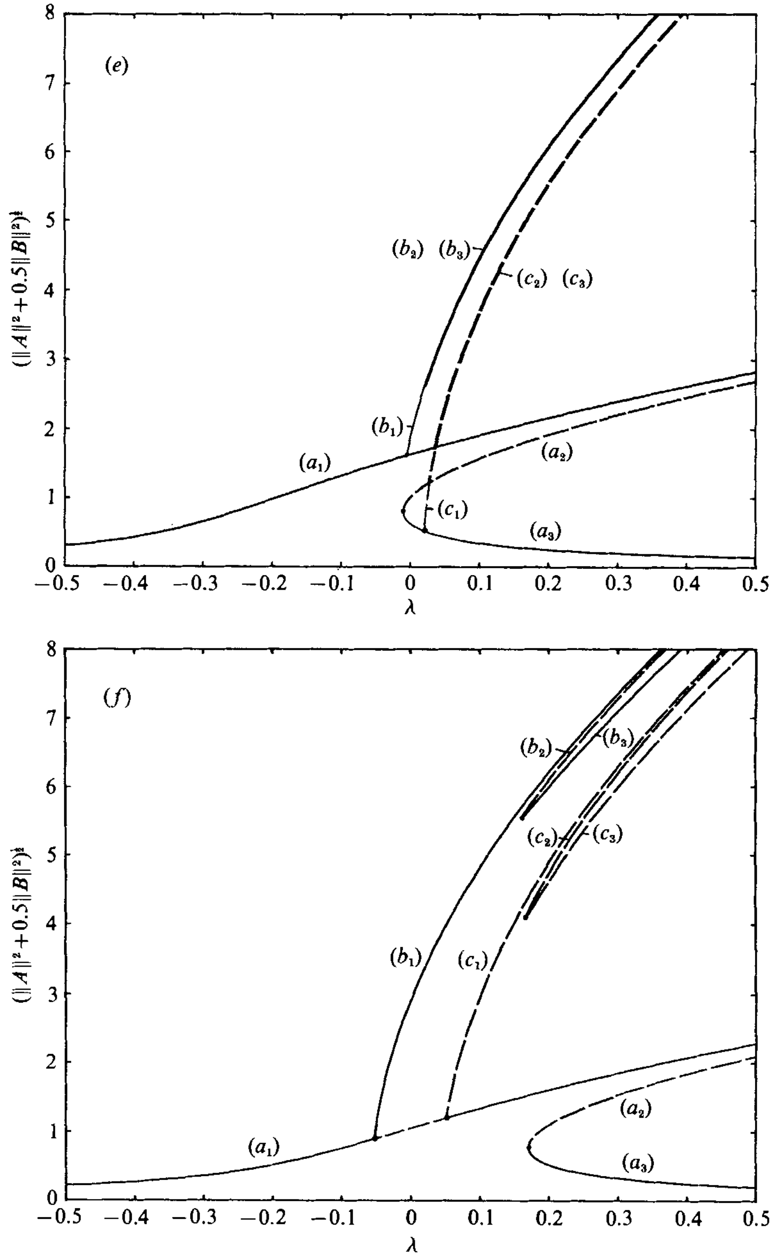

FIGURE 4. Bifurcation diagrams of the stationary solution amplitude $(\|A\|^2+0.5\|B\|^2)^{\frac{1}{2}}$ versus the excitation detuning parameter λ for $n = 1$, $l = 0.248602$, $\epsilon = 0.009072$ and (*a*) $h = 1.5$; (*b*) 1.6; (*c*) 1.7; (*d*) 1.9; (*e*) 2.2; (*f*) 4.0. The solid and broken lines are respectively the stable and unstable solutions and the bifurcation points are marked by solid dots.

dimensional wave becomes unstable, the amplitude of the transverse wave is not the maximum along the entire branch (b_3). The amplitude of the cross-wave continues to increase until $\lambda = \lambda_3$ and then decreases to zero at $\lambda = \lambda_4$ where the family of three-dimensional waves ends. Branch (c_1) is another family of stable three-dimensional waves which bifurcates from the two-dimensional longitudinal wave family (a_1) in

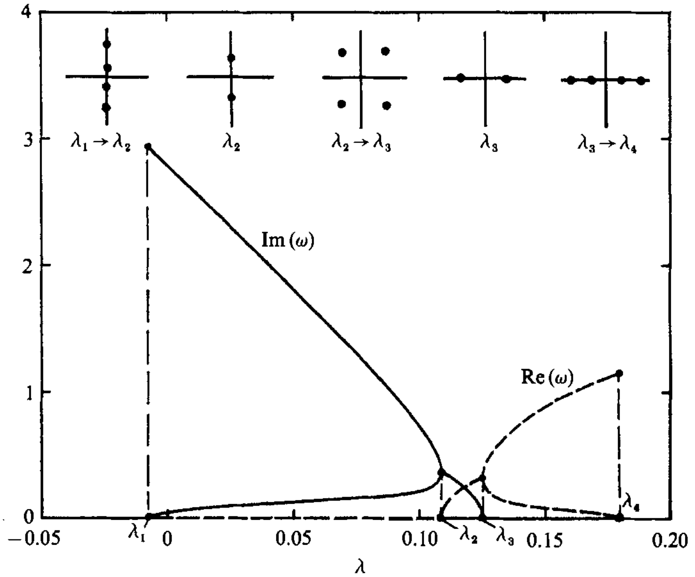

FIGURE 5. Variations of the real and imaginary parts of the eigenvalue ω along branch (b_3) of figure 4(*b*) for $h = 1.6$. Pitchfork bifurcation occurs at $\lambda = \lambda_1$ and Hamiltonian–Hopf bifurcation occurs at $\lambda = \lambda_2$.

the reverse direction to branch (b_3). Two inverse pitchfork bifurcations, branch (b_1) bifurcating from (a_1), and (c_3) from (a_3) are all unstable wave families.

Figures 4(*c*) and 4(*d*) are bifurcation diagrams for $h = 1.7$ and 1.9. Similar to the cases of $h = 1.5$ and 1.6, the stable three-dimensional family bifurcates from branch (a_3) and ends at branch (a_1). Hamiltonian–Hopf bifurcation occurs on the (b_3) branch where the three-dimensional wave becomes unstable. Unlike the case of $h = 1.5$ and 1.6, however, the branch (b_1) which bifurcates from the (a_1) longitudinal wave is stable for the present depths. All the families of the stationary solution (5.9*c*) are unstable.

For the deep water case $h = 4.0$ (figure 4*f*), both three-dimensional wave families (5.9*b*) and (5.9*c*) bifurcate from the (a_1) branch of longitudinal waves. On the stable branch (b_1), both the longitudinal and transverse waves grow monotonically with increasing detuning parameter λ. The transverse wave grows faster than the longitudinal wave near the bifurcation, and then reaches the same growth rate as λ increases. The amplitude of the transverse wave finally increases to about 2.7 times that of the longitudinal wave. The other two solutions of (5.9*b*), one stable and one unstable branch, which are separated by a turning point, make up the family (b_2). On the stable branch, starting from the turning point, the amplitude of the longitudinal wave decreases while the amplitude of the transverse wave increases and dominates the three-dimensional wave motion. It is possible that some of the steady-state cross-waves observed by Lin & Howard are on this stable wave family which is more visible physically than the first stable branch (b_1).

Bifurcation diagram figure 4(*e*) is the transition between the cases of intermediate depths (figure 4(a–d)) and deep water (figure 4*f*). The three branches of both the families (5.9*b*) and (5.9*c*) are indistinguishable in the figures. As in the case of $h = 4.0$, branch (b_1) of family (5.9*b*) bifurcates from branch (a_1) of the longitudinal wave. On the other hand, the three unstable branches (c_1, c_2, c_3) of family (5.9*c*) bifurcate from branches (a_1, a_2, a_3) respectively, similar to the case of $h = 1.8$.

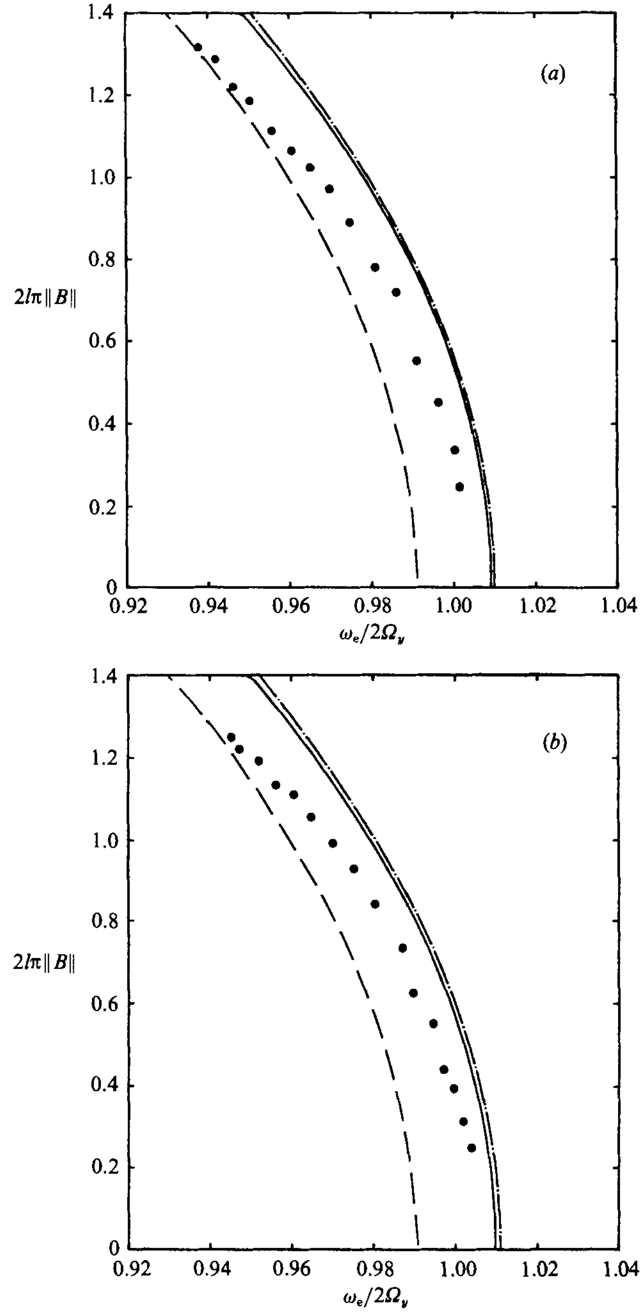

FIGURE 6. Comparisons of the frequency-response relationship for stationary transverse waves between the present analytic results and Lin & Howard's (1960) experimental measurements (circles) for (*a*) $L = 6$ in., $W = 24.1875$ in., $H = 24$ in., $2\theta = 0.279°$; and (*b*) $L = 12$ in., $W = 24.1875$ in., $H = 20$ in., $2\theta = 0.990°$. The solid and broken lines are stable and unstable stationary solutions of (4.4). The chain line is the stable cross-wave stationary solution (5.10*b*).

Through a careful and difficult bifurcation analysis, it may, in principle, be possible to identify regions of the frequency parameter in figure 4 for which more complex motions are likely to occur. In the present case, at least one stable solution exists for any value of λ and it is not immediately evident where chaotic solutions are most probable. From later Poincaré section plots (figure 12 for $\lambda = 0.1$ and figure 13 for $\lambda = 0.2$), chaotic motions appear to be more widespread near $\lambda = 0.2$ than $\lambda = 0.1$, corresponding to the somewhat more complex stationary solution picture near the higher frequency in figure 4(*b*). A more quantitative prediction based on bifurcation analyses may not be possible.

Figure 6 shows comparison between the theoretical results and Lin & Howard's experimental data for the transverse stationary wave amplitude for the cases of $L = 6$ in., $W = 24.1875$ in., $H = 24$ in., $l = 0.248062 \approx \frac{1}{4}$, $2\theta = 0.279°$ (figure 6*a*), and $L = 12$ in., $W = 24.1875$ in., $H = 20$ in., $l = 0.496124 \approx \frac{1}{2}$, $2\theta = 0.990°$ (figure 6*b*) respectively. For the $l \approx \frac{1}{4}$ case, both longitudinal and transverse waves are first spatial harmonic modes, while for $l \approx \frac{1}{2}$, the oscillation of the first-mode transverse wave is associated with the second-mode longitudinal wave. The solid and broken lines represent respectively the stable and unstable analytic results which consider the parametric resonance only (§4). The chain line is for the amplitude of the stable transverse wave response for which the interaction between resonant longitudinal and transverse waves is included. Similar to figure 2, but somewhat less satisfactory, the figures again show overpredictions of the theoretical response amplitude for both comparisons. One explanation for the discrepancy is the difficulty of separating the longitudinal and transverse wave components from the wave-gauge measurements which was done graphically by Lin & Howard. The possible importance of dissipation again cannot be ruled out.

5.3. *Regular and chaotic behaviour*

To obtain some understanding of the nonlinear evolution, (5.5), or equivalently (5.8), are integrated numerically. A fourth-order Runge–Kutta scheme with a typical time step $\Delta\tau = 0.005$ is used for the numerical simulations. For all the numerical results, the value of the Hamiltonian is conserved to nine decimal places. Depending on the parameters selected, and the initial conditions, the simulated temporal trajectories may exhibit either regular (periodic and quasi-periodic) or chaotic behaviour.

Figures 7 and 8 show the temporal evolution for the case of $h = 1.6$, $\lambda = 0.2$, $l = 0.248062$, $\epsilon = 0.009072$, but with initial conditions $(C_a, D_a, C_b, D_b) = (0, -4.1373221, 0, 6)$ and $(0, -4.5269170, 4, 0)$ respectively. Both sets of initial conditions have the same Hamiltonian $\mathscr{H} = 9.0$. For the first set of initial conditions, the temporal evolution in figure 7 are regular (quasi-periodic). Since the two timescales τ_1 and τ_2 are combined into the shorter scale τ_1, the transverse wave modulates over a longer timescale than the longitudinal wave. The interactions between the two are relatively weak. When the initial conditions are changed (figure 8), the resulting evolution becomes aperiodic and chaotic. The resonant interactions between the longitudinal and transverse waves are quite apparent.

For the chaotic evolution, two solutions with slightly different initial conditions in general depart from each other at an exponential rate, and the differences in the initial conditions are manifested at a later time by vastly different dynamical states. Such a characteristic of sensitivity to initial conditions can be quantified in terms of Lyapunov characteristic exponents which measure the mean rate of exponential separation of neighbouring evolution trajectories. For numerical calculations, we adopt a renormalization scheme suggested by Benettin, Galgani & Strelcyn (1976) to

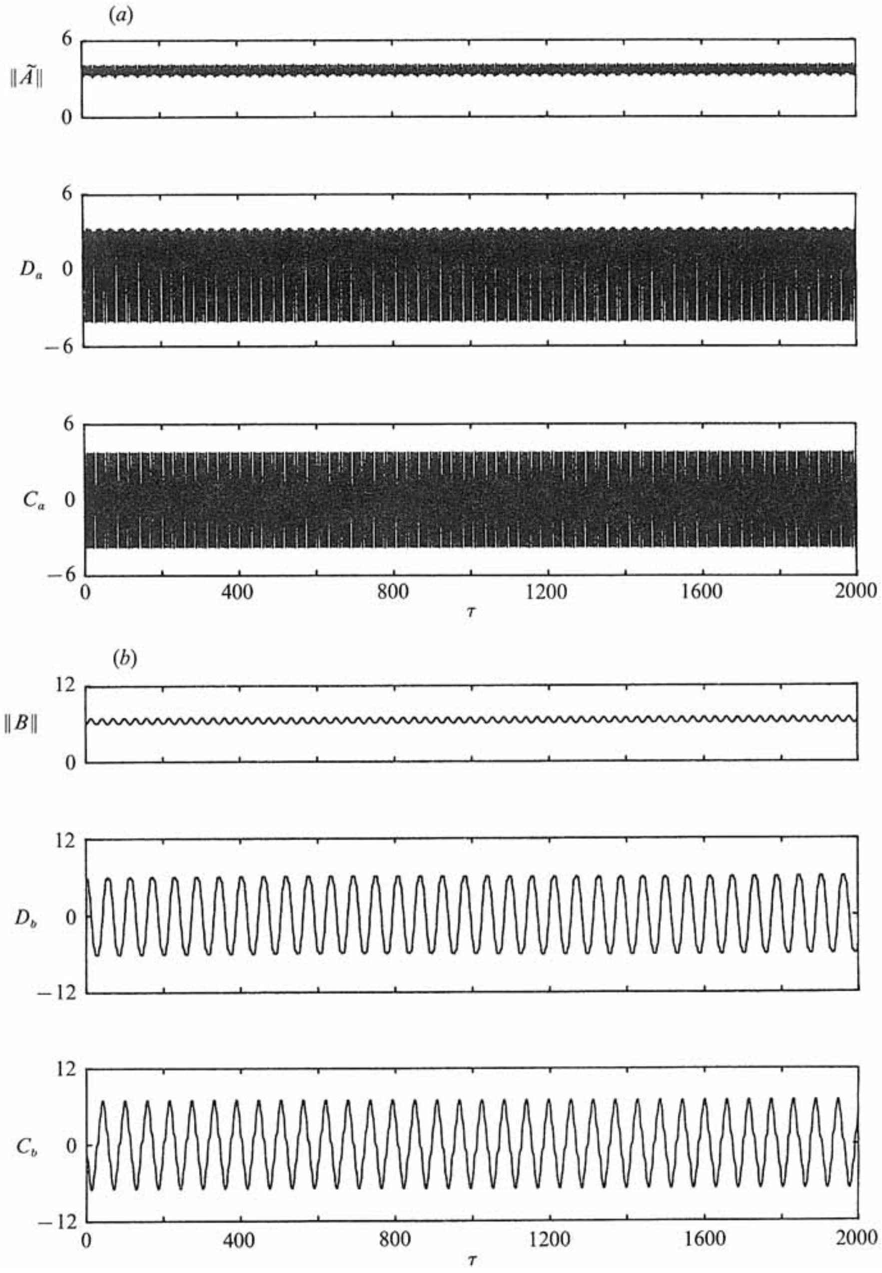

FIGURE 7. Time evolution of (*a*) the longitudinal wave envelope, and (*b*) the transverse wave envelope for $h = 1.6$, $\lambda = 0.2$, $l = 0.248062$, $\epsilon = 0.009072$ with the initial condition $(C_a, D_a, C_b, D_b) = (0, -4.137221, 0, 6)$.

compute the maximum Lyapunov exponent. Figure 9 shows the variation of the maximum Lyapunov exponent σ for the parameter values and the different initial conditions of figures 7 and 8. For the regular evolution (figure 7), it is seen that σ (triangles) decreases and eventually vanishes in the limit of large τ. For the chaotic motion of figure 8, however, σ (rectangles) approaches a positive finite value measuring the exponential divergence of neighbouring trajectories.

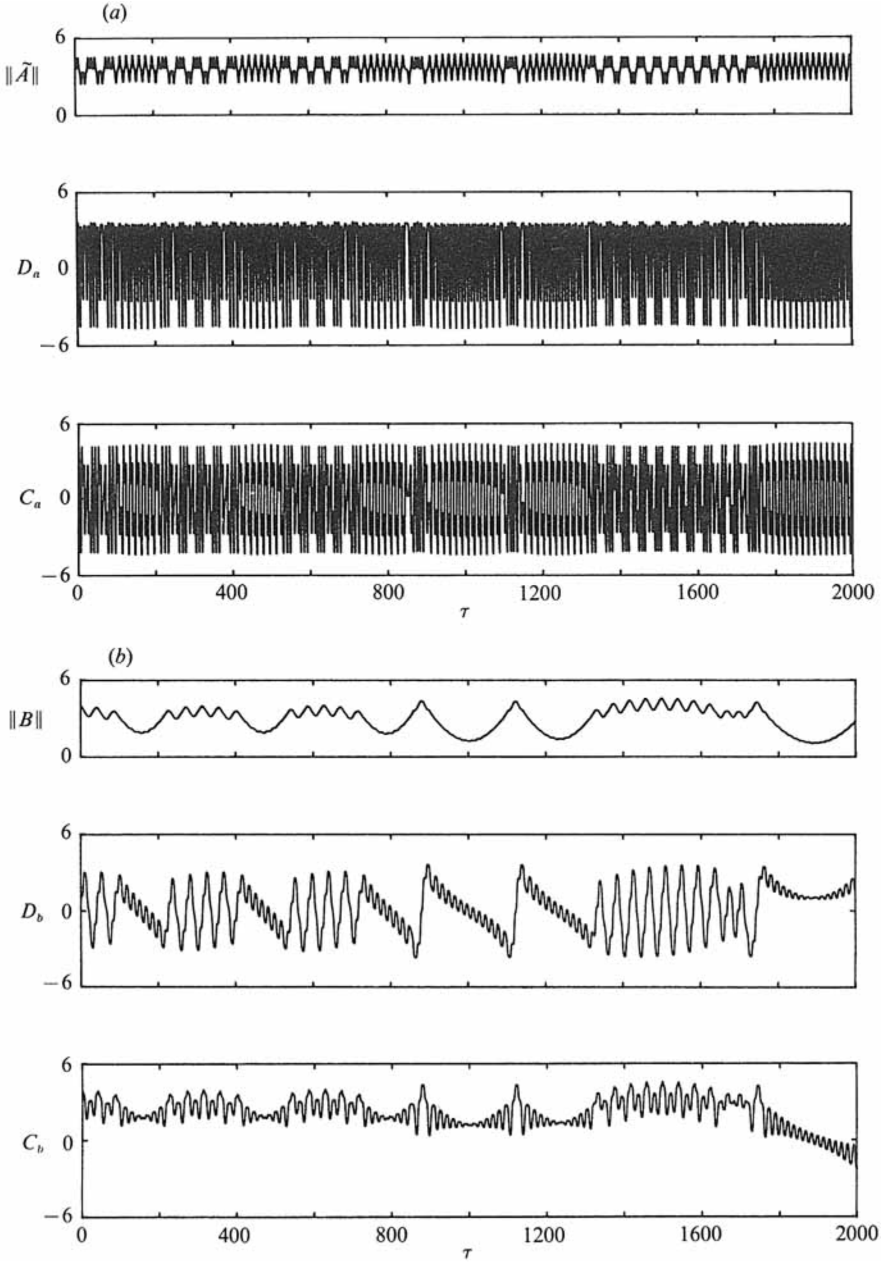

FIGURE 8. Time evolution of (*a*) the longitudinal wave envelope, and (*b*) the transverse wave envelope for $h = 1.6$, $\lambda = 0.2$, $l = 0.248062$, $\epsilon = 0.009072$ with the initial condition $(C_a, D_a, C_b, D_b) = (0, -4.526917, 4, 0)$.

Another characterization for regular and chaotic behaviour is the power spectrum of the evolution amplitude. From the numerical solution of the evolution over a time interval $N\Delta\tau$, the power spectrum can be estimated using fast Fourier transform according to

$$P_{a,b}(f_n) = \frac{2\Delta\tau}{N}\left\| \sum_{k=0}^{N-1} E_{a,b}(\tau_k)\,\omega(\tau_k)\exp\left(\mathrm{i}2\pi\frac{kn}{N}\right)\right\|^2, \tag{5.14}$$

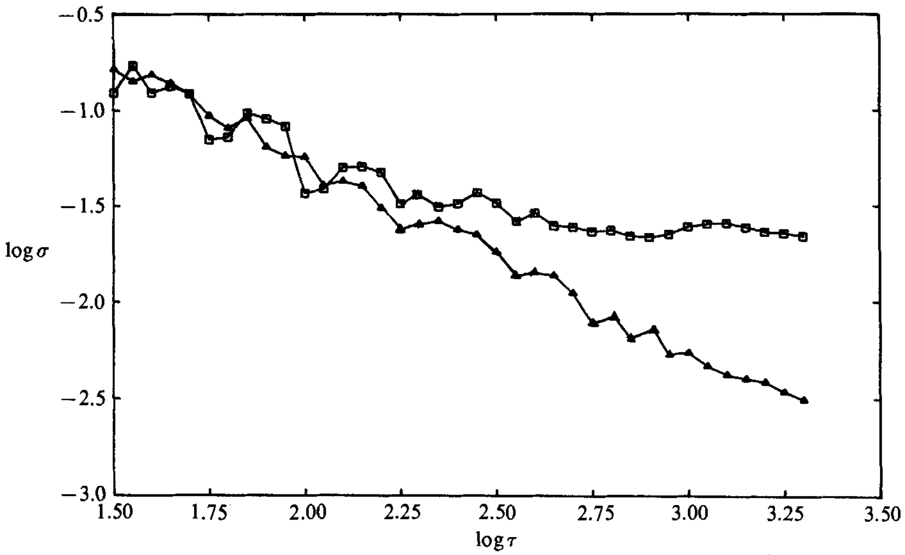

FIGURE 9. Variation of the maximum Lyapunov exponent σ with τ for the evolutions of figures 7 (triangles) and 8 (rectangles).

where $\tau_k = k\Delta\tau$ is the discrete time, $f_n = n/(N\Delta\tau)$ is the discrete frequency, and $w(\tau_k) = (\frac{2}{3})^{\frac{1}{2}}[1-\cos(2\pi k/N)]$ is the Hanning window function employed. The power spectra of the modulus $\|\bar{A}\|$ and $\|B\|$ for two sets of initial conditions of figures 7 and 8 are shown in figures 10 and 11. For the regular evolution, the power spectrum (figure 10) consists of a finite series of discrete spikes which corresponds to multiharmonic motions in the quasi-periodic evolution. For the chaotic evolution (figure 11) the spectrum exhibits broadband features characteristics of such motions.

To understand the global behaviour of the Hamiltonian system in phase space, we construct the two-dimensional first return map on the hypersurface $\Sigma_{\mathscr{H}}$ of codimension-one. Such a hypersurface is known as a Poincaré surface of section, which we choose for our problem to be defined by

$$\Sigma_{\mathscr{H}} = \{(C_a, D_a, C_b, D_b) : C_a = 0, \frac{\mathrm{d}C_a}{\mathrm{d}\tau} > 0, \mathscr{H} = \mathscr{H}(C_a, C_b, D_a, D_b; \lambda, h, l, n)\}. \quad (5.15)$$

On the Poincaré section, a fixed point corresponds to a periodic trajectory, points lying on smooth curves (invariant curves) belong to a quasi-periodic orbit, while those belonging to a chaotic orbit will appear to fill a region.

Figure 12 shows the Poincaré sections for the same geometric parameters as those for figures 7 and 8 but with $\lambda = 0.1$ and for Hamiltonian values $\mathscr{H} = 2.0$, 4.0 and 6.0 respectively. For the lowest energy level $\mathscr{H} = 2.0$, the phase portrait figure 12(*a*) appears completely regular: an elliptic fixed point at the origin surrounded by a nested sequence of invariant curves. As the energy level increases, for example figure 12(*b*) for $\mathscr{H} = 4.0$, a chaotic region is seen between the inner and outer regular phase space. When the energy level is further raised, the outermost energy surface shrinks in the phase space and regular motions become predominant again as shown in figure 12(*c*) for $\mathscr{H} = 6.0$. We call this scenario the 'banded-energy' phenomenon since chaotic motions appear to be limited to an interval (or band) of energy values.

Completely different pictures emerge as one or more of the other physical parameters are altered. For illustration, we keep the same geometry and detuning

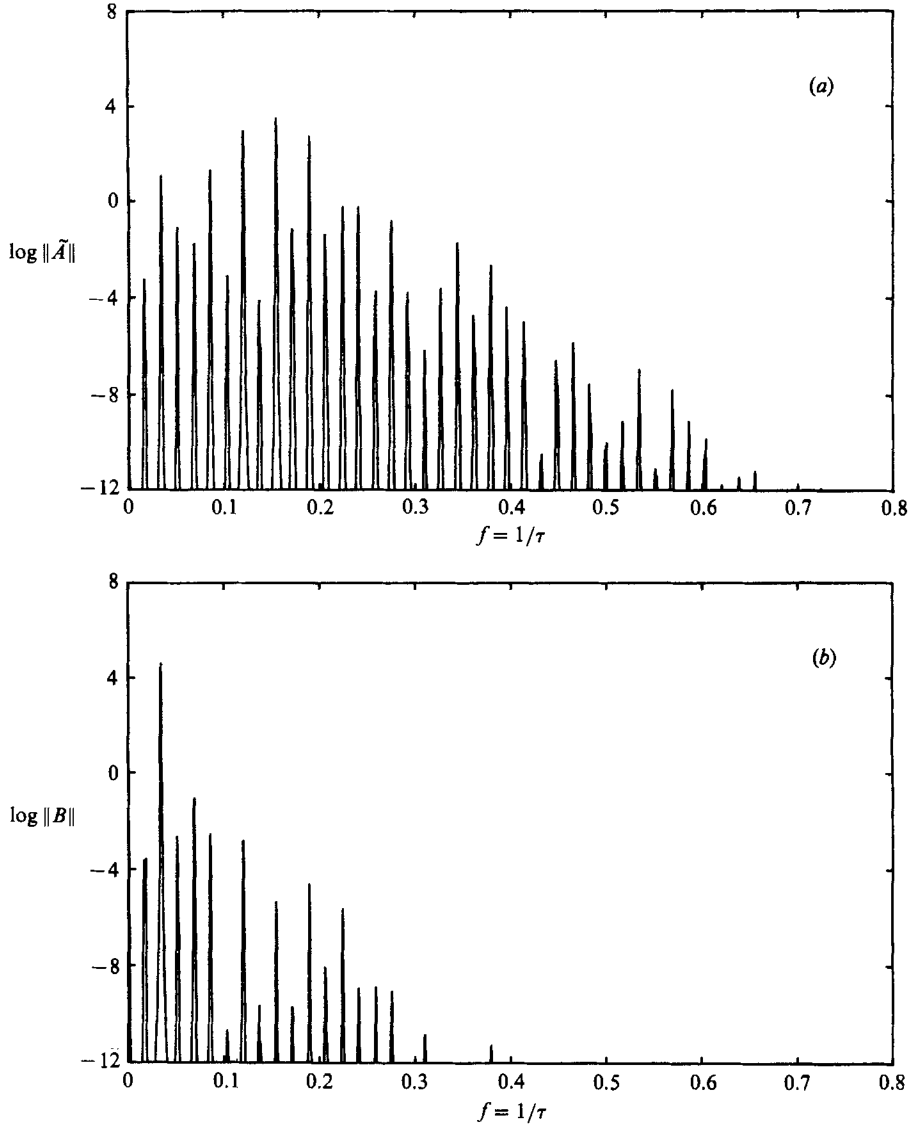

FIGURE 10. Power spectrum of the evolution amplitudes (*a*) $\|\tilde{A}\|$ and (*b*) $\|B\|$ in figure 7.

value of $\lambda = 0.2$ as figures 7 and 8, and consider the Poincaré sections for energy levels corresponding to $\mathscr{H} = 8.0$, 9.0, 10.0 and 11.968215 respectively. The fourth value of $\mathscr{H}$ is the Hamiltonian of the two-dimensional longitudinal stationary wave (branch a_1 in figure 4*a*) with a perturbation of $0.001(\delta D_{a0})$. The phase portraits in figure 13(*a*) for $\mathscr{H} = 8.0$ are completely regular. For somewhat higher energies, say $\mathscr{H} = 9.0$, we see that the elliptic fixed point at the origin loses its stability, becoming hyperbolic, and gives rise to two elliptic fixed points (figure 13*b*). Note that the simulations of figures 7 and 8 correspond to this case and the resulting regular and chaotic evolutions starting from the two different initial conditions are evident from figure 13(*b*). As the energy level is further increased, a large chaotic zone occupies most of the energy surface while the region of regular orbits shrinks as shown in figure 13(*c*) for $\mathscr{H} = 10.0$. When $\mathscr{H}$ reaches close to its maximum value, for example for

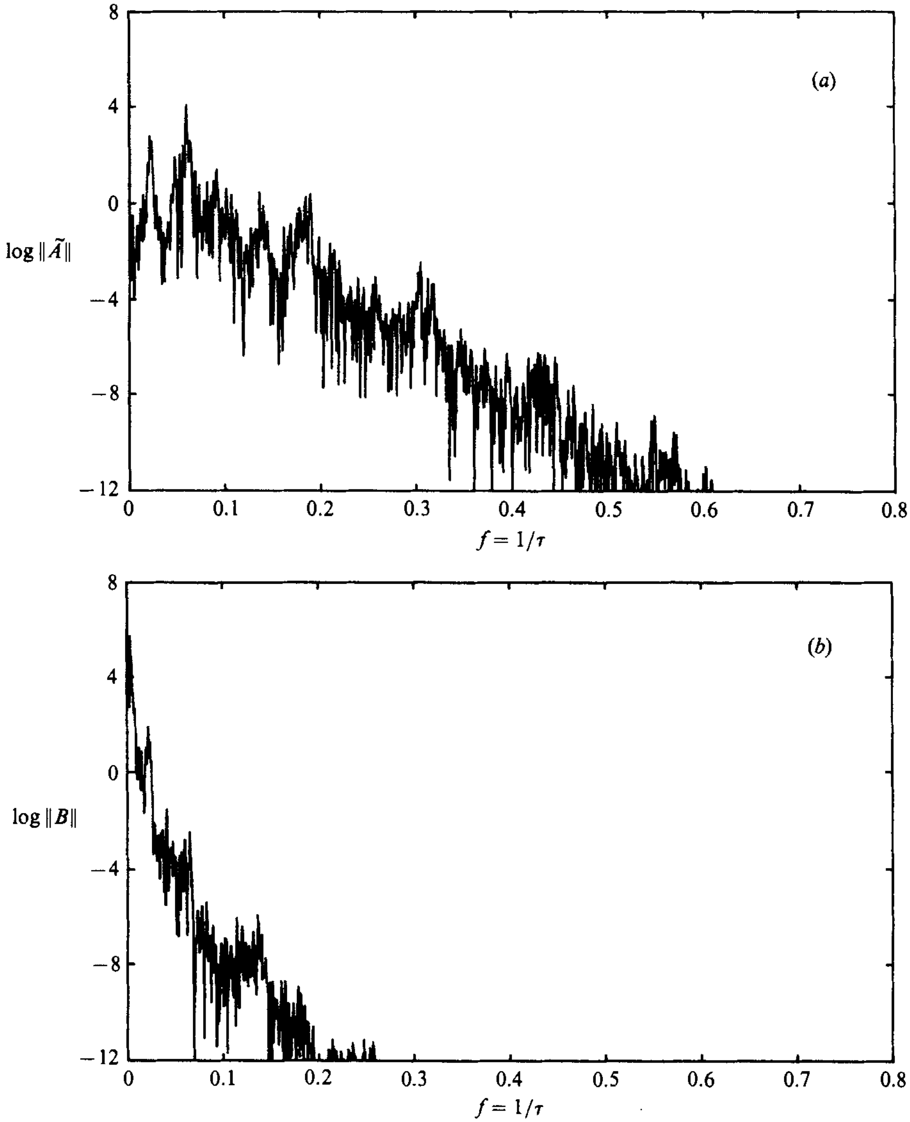

FIGURE 11. Power spectrum of the evolution amplitudes (a) $\|\tilde{A}\|$ and (b) $\|B\|$ in figure 8.

$\mathscr{H} = 11.968215$ in figure 13 (d), the elliptic fixed point at the origin reappears and the outermost energy surface forms a shell-like shape occupied mostly by chaotic orbits surrounded by a small layer of regular orbits. We refer to this as the 'critical-energy' phenomenon because there seems to be a critical energy level beyond which chaotic orbits dominate the phase space.

As we have seen, the present nonlinear dynamical system possesses remarkably rich and varied solution features depending in subtle ways on the physical parameters, h, l, n, λ and ϵ, the total energy, $\mathscr{H}$, as well as the specific initial phases of the motions. Given the large number of variables, a more global understanding of the problem, for example a criterion for the onset of widespread chaos, would be most useful.

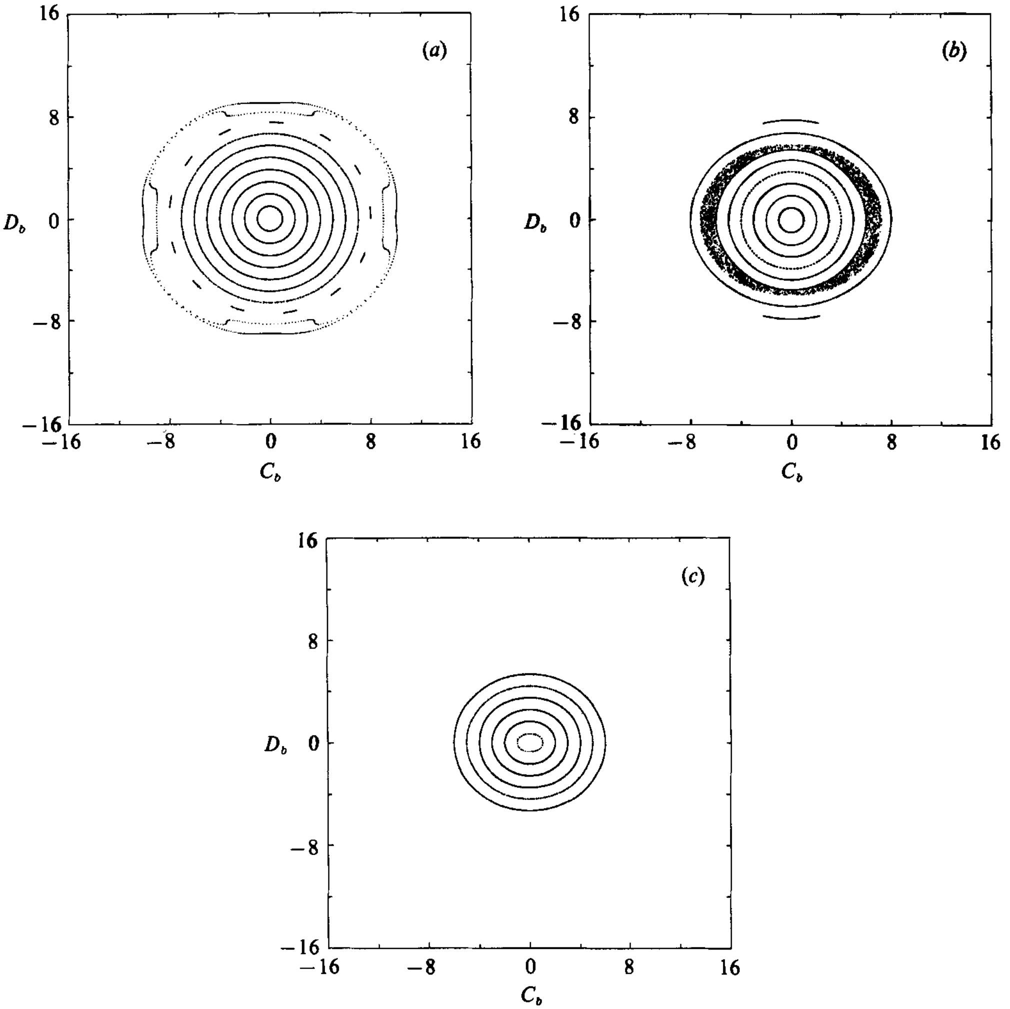

FIGURE 12. Poincaré sections for $h = 1.6$, $\lambda = 0.1$, $l = 0.248062$, $\epsilon = 0.009072$ on energy surfaces corresponding to (a) $\mathscr{H} = 2.0$; (b) 4.0; (c) 6.0.

6. Resonance overlap as a criterion for the onset of widespread chaos

In the preceding section we characterize the dynamical features (regular and chaotic) of the Hamiltonian system (5.8) by the Lyapunov characteristic exponent and power spectrum of the evolutions. Both of these only identify and quantify the *local* nature of the dynamical system. The global behaviour of the Hamiltonian system with two degrees of freedom almost always exhibits a divided phase space: for some regimes the evolutions are regular and for others chaotic, as shown for example in figures 12 and 13. To explore the global dynamic behaviour of the system directly in the large parameter space of h, l, λ, ϵ, n and $\mathscr{H}$ plus the relative phases is clearly difficult if not prohibitive. It would be valuable to obtain an estimate in terms of the physical parameters of the likelihood, say, of chaotic motions without resorting to detailed time-consuming numerical simulations in the entire phase and parameter space.

One approximate but effective technique for giving estimates of the onset of chaos for a large class of Hamiltonian systems is the method of resonance overlap due to

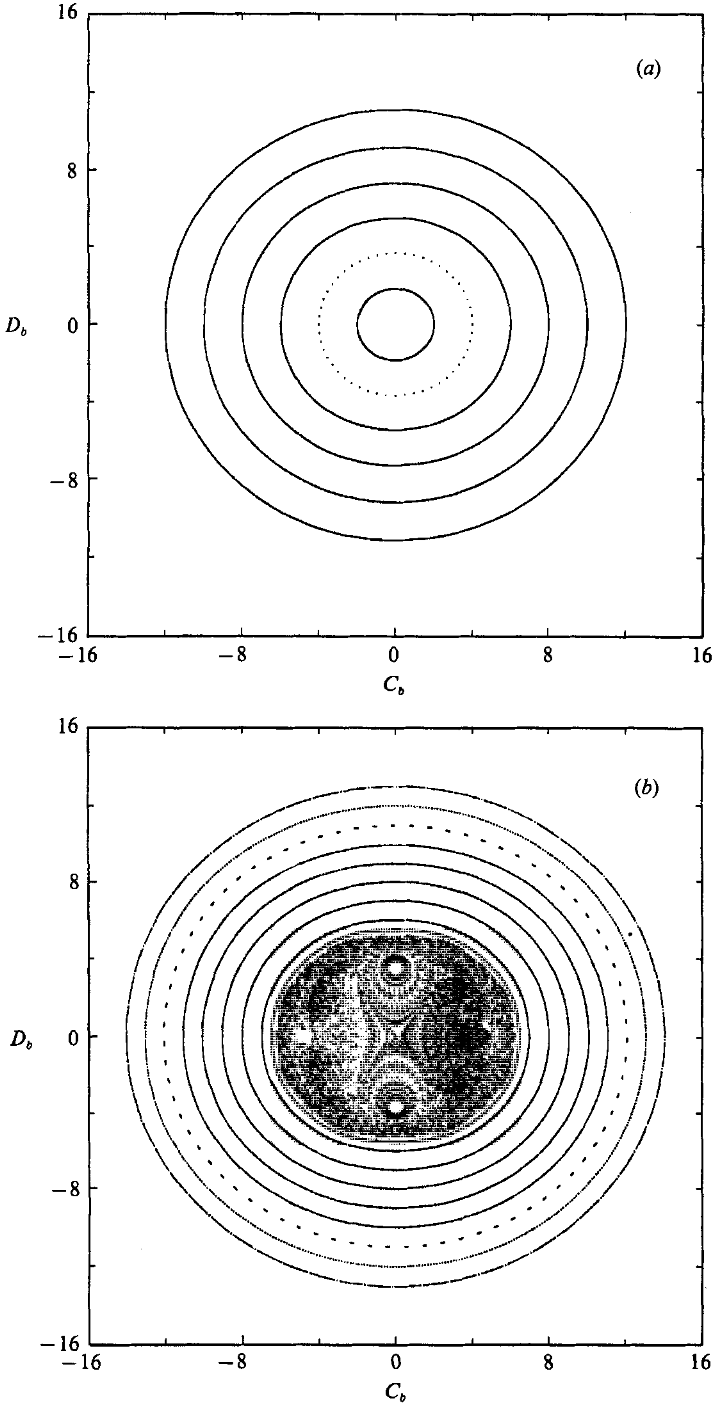

FIGURE 13(a,b). For caption see facing page.

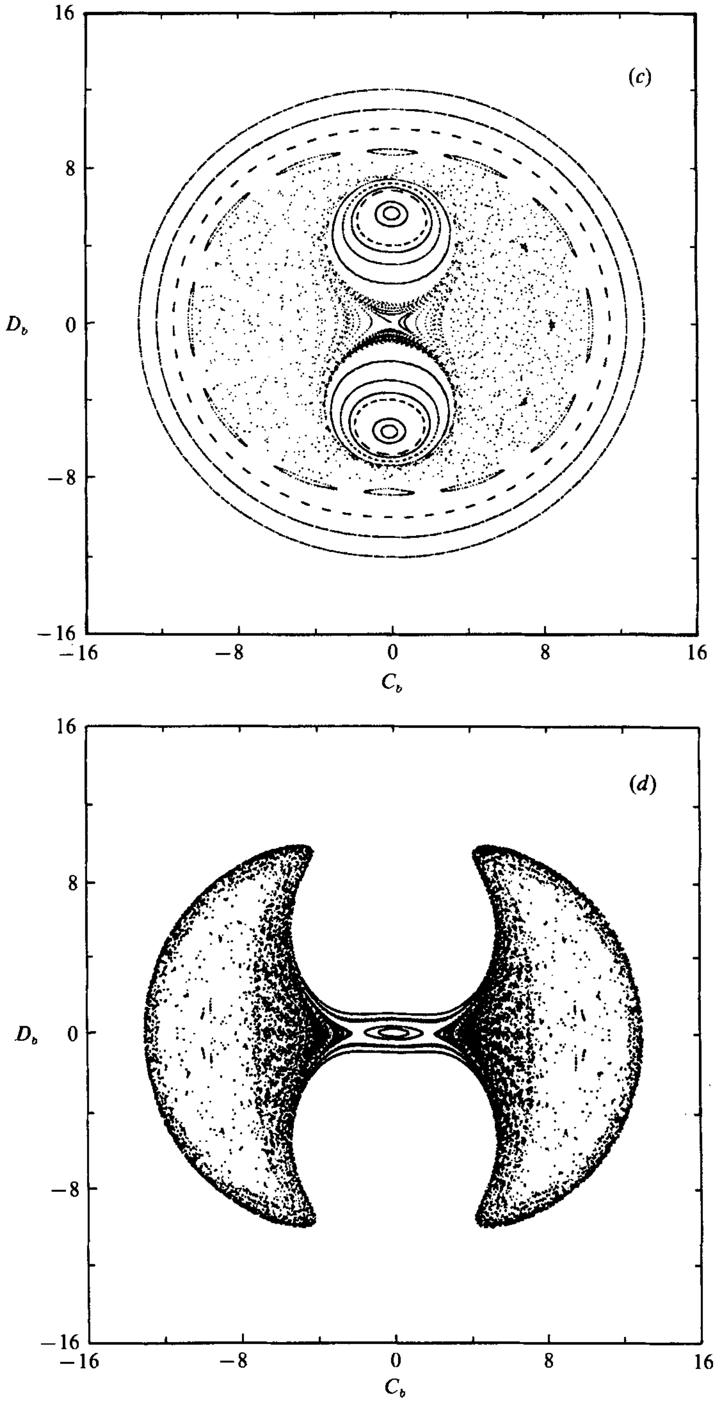

FIGURE 13. Poincaré sections for $h = 1.6$, $\lambda = 0.2$, $l = 0.248062$, $\epsilon = 0.009072$ on energy surfaces corresponding to (*a*) $\mathscr{H} = 8.0$; (*b*) 9.0; (*c*) 10.0; (*d*) 11.968215.

Chirikov (1979). The basic supposition of the method is that the destruction of tori and the appearance of widespread chaos can be attributed to the overlapping of the primary nonlinear resonances. According to the Kolmogorov–Arnol'd–Moser (KAM) theorem (Arnol'd 1978), for an integrable system, those invariant curves with sufficiently incommensurate winding numbers persist under small perturbations. As the strength of the perturbation increases, neighbouring resonance zones will interact and chaotic motion is confined to a narrow regime around the separatrices bounding the resonance zones. As two resonance zones grow and eventually overlap, invariant curves between them will be destroyed, resulting in the onset of widespread chaos. The method of resonance overlap postulates that the last invariant curve between two lowest-order resonances is destroyed when the sum of the half-widths equals the distance between the resonance centres. A major approximation is that the width of each resonance zone can be calculated independently of all the others. This simple criterion results in a conservative estimate, i.e. a sufficient condition, for chaos because chaotic motion may result from interactions of the secondary resonances lying between the two primary resonances before the two primary resonance zones actually touch. Nevertheless the criterion yields a practical estimate for the critical parameters governing the transition to widespread chaos.

Applying the canonical transformation:

$$\tilde{A} = \mathrm{i}(2I_a)^{\frac{1}{2}}\exp(\mathrm{i}\theta_a), \quad B = \mathrm{i}(2I_b)^{\frac{1}{2}}\exp(\mathrm{i}\theta_b),$$

where $I_{a,b}$ and $\theta_{a,b}$ are action and angle variables, the Hamiltonian (5.7) takes the new form:

$$\mathscr{H} = \mathscr{H}_0 + \mathscr{H}_a + \mathscr{H}_b, \tag{6.1a}$$

$$\mathscr{H}_0 = -\frac{1}{\mu}(-\gamma_a I_a - \gamma_b I_b + \tilde{\Gamma}_a I_a^2 + \tilde{\Gamma}_b I_b^2 + 2\tilde{\Sigma} I_a I_b), \tag{6.1b}$$

$$\mathscr{H}_a = -\frac{\tilde{\delta}}{\mu}(2I_a)^{\frac{1}{2}}\cos\theta_a, \quad \mathscr{H}_b = \frac{\tilde{\beta}}{\mu} I_b \cos 2\theta_b. \tag{6.1c, d}$$

The new form of the Hamiltonian consists of an integrable part $\mathscr{H}_0$ and two non-integrable perturbations $\mathscr{H}_a$ and $\mathscr{H}_b$ responsible for the two primary resonances caused by the forced and parametric resonances respectively. The strategy is to calculate the resonance conditions and the widths of the resonance zones of $\mathscr{H}_A = \mathscr{H}_0 + \mathscr{H}_a$ and $\mathscr{H}_B = \mathscr{H}_0 + \mathscr{H}_b$ independently, and find the perturbation strength at which these two primary resonances touch. That the calculation can be done for each resonance in isolation is clearly a major approximation in the method of resonance overlap.

For a general Hamiltonian $\mathscr{H}(\boldsymbol{I}, \boldsymbol{\theta})$, where $\boldsymbol{I}$ and $\boldsymbol{\theta}$ are the vectors of action and angle variables, a resonance arises at those values of $\boldsymbol{I} = \boldsymbol{I}^{\mathrm{r}}$ where the frequencies are commensurate. That is, there exists a vector $\boldsymbol{k}$ with irreducible integer components such that

$$\boldsymbol{k}\cdot\boldsymbol{\omega}^{\mathrm{T}}(\boldsymbol{I}^{\mathrm{r}}) = \boldsymbol{k}\cdot[\boldsymbol{\nabla}_{I}\mathscr{H}(\boldsymbol{I})]^{\mathrm{T}}_{I=I^{\mathrm{r}}} = 0, \tag{6.2}$$

where $\boldsymbol{k}$ is called the resonance vector. In general, for a Hamiltonian system of N degrees of freedom, each resonance vector defines an $(N-1)$-dimensional resonance surface in the N-dimensional action variables space. For the Hamiltonian $\mathscr{H}_A$, the resonance vector $\boldsymbol{k} = (1,0)$, which gives the resonance condition

$$2\tilde{\Gamma}_a I_a^{\mathrm{r}} + 2\tilde{\Sigma} I_b^{\mathrm{r}} - \gamma_a = 0. \tag{6.3}$$

Similarly for the Hamiltonian $\mathscr{H}_B$ with resonance vector $\boldsymbol{k} = (0, 2)$, the resonance condition is

$$2\tilde{\Sigma} I^{\mathrm{r}}_a + 2\tilde{\Gamma}_b I^{\mathrm{r}}_b - \gamma_b = 0. \tag{6.4}$$

The next step is to transform the Hamiltonians $\mathscr{H}_A$ and $\mathscr{H}_B$ into canonical pendulum Hamiltonians. We proceed by introducing the generating function

$$F(\boldsymbol{J}, \boldsymbol{\theta}) = (\boldsymbol{I}^{\mathrm{rT}} + \boldsymbol{J} \cdot \boldsymbol{\mu}) \cdot \boldsymbol{\theta}^{\mathrm{T}}, \tag{6.5}$$

where $\boldsymbol{J}$ is the new vector of action variables and $\boldsymbol{\mu}$ is a constant matrix. The new angle variables are then given by

$$\boldsymbol{\psi}^{\mathrm{T}} = \boldsymbol{\mu} \cdot \boldsymbol{\theta}^{\mathrm{T}}, \tag{6.6}$$

where the kth element is the resonant phase $\psi_k = \boldsymbol{k} \cdot \boldsymbol{\theta}^{\mathrm{T}}$, and is slow relative to the other phases. Following Tabor (1981), we choose the constant matrix $\boldsymbol{\mu}$ in such a way that $\psi_j = \theta_j$ for $j \neq k$. The new angle variables $\psi_j = \theta_j, j \neq k$ therefore are linearly independent and are fast relative to the resonant phase ψ_k. For the Hamiltonian $\mathscr{H}_A$, the transformations between the original and new action and angle variables are

$$\boldsymbol{I}^{\mathrm{T}} = \begin{Bmatrix} I_a \\ I_b \end{Bmatrix} = \boldsymbol{I}^{\mathrm{rT}} + \boldsymbol{J} \cdot \boldsymbol{\mu}, \quad \boldsymbol{\theta}^{\mathrm{T}} = \begin{Bmatrix} \theta_a \\ \theta_b \end{Bmatrix} = \boldsymbol{\mu}^{-1} \cdot \boldsymbol{\psi}^{\mathrm{T}}. \tag{6.7a, b}$$

Transforming the Hamiltonian $\mathscr{H}_A$ to the new action and angle variables, averaging the Hamiltonian over the fast variables $\psi_j, j \neq k$, and expanding $\mathscr{H}_0(I_a, I_b)$ about the resonant actions $\boldsymbol{I} = \boldsymbol{I}^{\mathrm{r}} = (I^{\mathrm{r}}_a, I^{\mathrm{r}}_b)$ yields

$$\begin{aligned} \bar{\mathscr{H}}_A \approx{} & \mathscr{H}_0(I^{\mathrm{r}}_a, I^{\mathrm{r}}_b) - \frac{\tilde{\delta}}{\mu}(2I^{\mathrm{r}}_a)^{\frac{1}{2}} \cos \psi_a \\ & + \left[J_a \frac{\partial \mathscr{H}_0}{\partial I_a} + J_b \frac{\partial \mathscr{H}_0}{\partial I_b} + \tfrac{1}{2} J_a^2 \frac{\partial^2 \mathscr{H}_0}{\partial I_a^2} + J_a J_b \frac{\partial^2 \mathscr{H}_0}{\partial I_a \partial I_b} + \tfrac{1}{2} J_b^2 \frac{\partial^2 \mathscr{H}_0}{\partial I_b^2} \right]_{I = (I^{\mathrm{r}}_a, I^{\mathrm{r}}_b)}. \end{aligned} \tag{6.8}$$

Dropping the constant term $\mathscr{H}_0(I^{\mathrm{r}}_a, I^{\mathrm{r}}_b)$ and applying the resonance condition $\partial \mathscr{H}_0 / \partial I_a = 0$, $\bar{\mathscr{H}}_A$ becomes

$$\bar{\mathscr{H}}_A \approx -\frac{\tilde{\Gamma}_a}{\mu} J_a^2 - \frac{\tilde{\delta}}{\mu}(2I^{\mathrm{r}}_a)^{\frac{1}{2}} \cos \psi_a + \left[J_b \frac{\partial \mathscr{H}_0}{\partial I_b} + J_a J_b \frac{\partial^2 \mathscr{H}_0}{\partial I_a \partial I_b} + \tfrac{1}{2} J_b^2 \frac{\partial^2 \mathscr{H}_0}{\partial I_b^2} \right]_{I = (I^{\mathrm{r}}_a, I^{\mathrm{r}}_b)}. \tag{6.9}$$

The next approximation of the method of resonance overlap is to assume that the net contribution from the last three terms is small, and we finally obtain the pendulum form of the resonant Hamiltonian as

$$\overline{\mathscr{H}^{\mathrm{r}}_A} = -\frac{\tilde{\Gamma}_a}{\mu} J_a^2 - \frac{\tilde{\delta}}{\mu}(2I^{\mathrm{r}}_a)^{\frac{1}{2}} \cos \psi_a. \tag{6.10}$$

The resonance half-width is then given by

$$\Delta J = \left(\frac{2\tilde{\delta}}{\tilde{\Gamma}_a} \right)^{\frac{1}{2}} (2I^{\mathrm{r}}_a)^{\frac{1}{4}}. \tag{6.11}$$

From this we can obtain the vector of resonance widths in the original action variables as

$$\Delta \boldsymbol{I}^{\mathrm{T}} = \begin{Bmatrix} \Delta I_a \\ \Delta I_b \end{Bmatrix} = \boldsymbol{k}^{\mathrm{T}} \cdot \Delta \boldsymbol{J} = \begin{Bmatrix} (2\tilde{\delta}/\tilde{\Gamma}_a)^{\frac{1}{2}} (2I^{\mathrm{r}}_a)^{\frac{1}{4}} \\ 0 \end{Bmatrix}. \tag{6.12}$$

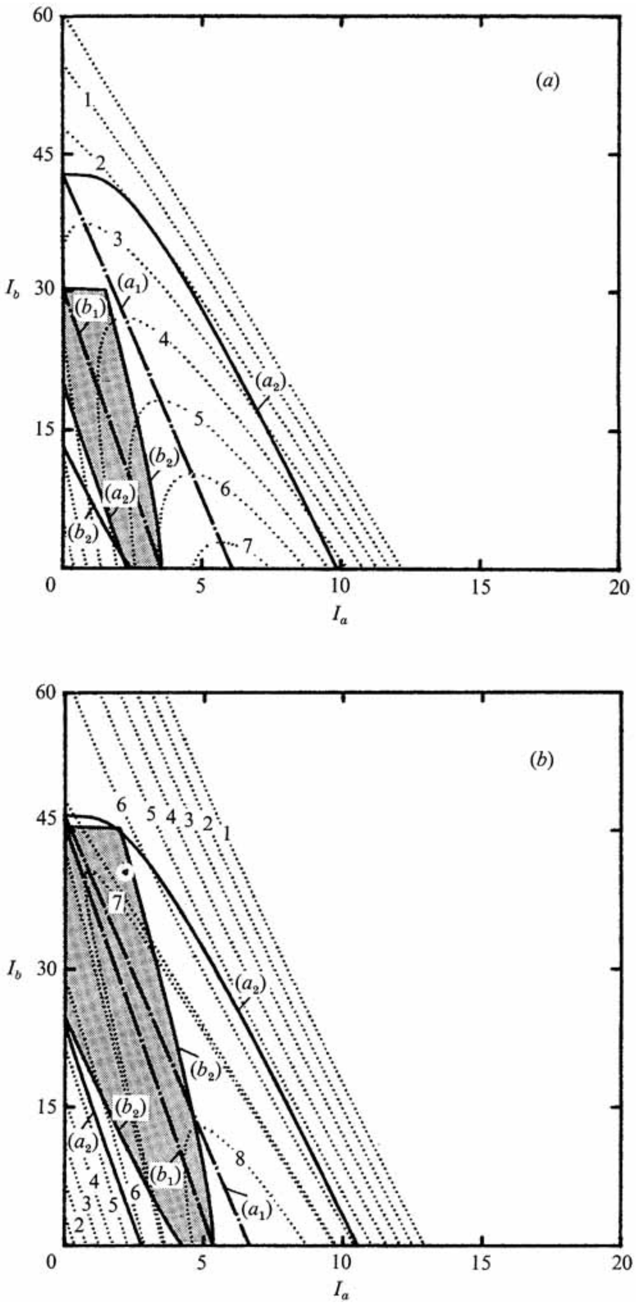

FIGURE 14 (a, b). For caption see facing page.

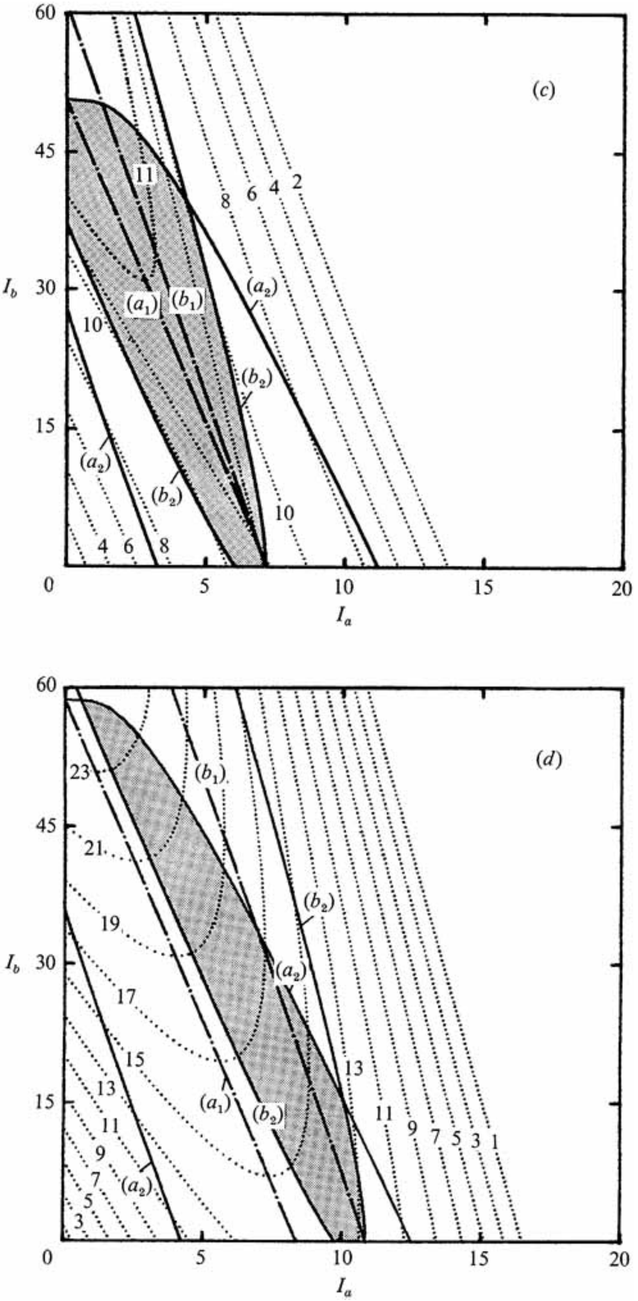

FIGURE 14. Resonance overlap diagrams for $h = 1.6$, $l = 0.248062$, $\epsilon = 0.009072$ with (*a*) $\lambda = 0.1$; (*b*) 0.15; (*c*) 0.2; (*d*) 0.3. The chain lines (a_2) and (b_1) are resonance conditions for $\mathscr{H}_A$ and $\mathscr{H}_B$, and the thick solid lines (a_2) and (b_2) denote resonance boundaries of $\mathscr{H}_A$ and $\mathscr{H}_B$ respectively. The shaded area is the overlap region of the two resonances. The dotted lines are level curves of constant $\mathscr{H}_0$.

Similarly, for the Hamiltonian $\mathscr{H}_B$, the corresponding canonical pendulum resonant Hamiltonian is

$$\overline{\mathscr{H}^{\mathrm{r}}_B} = -\frac{8\tilde{\Gamma}_b}{\mu} J_b^2 - \frac{-\tilde{\beta}}{\mu} I_b^{\mathrm{r}} \cos\psi_b, \tag{6.13}$$

and the resonance half-width is

$$\Delta J = \left(\frac{-\tilde{\beta}}{2\tilde{\Gamma}_b} I_b^{\mathrm{r}}\right)^{\frac{1}{2}}, \tag{6.14}$$

which gives the width of resonance in the original action variable as

$$\Delta I^{\mathrm{T}} = \left\{\begin{matrix} 0 \\ (-2\tilde{\beta} I_b^{\mathrm{r}}/\tilde{\Gamma}_b)^{\frac{1}{2}} \end{matrix}\right\}. \tag{6.15}$$

The above analysis can be applied graphically to determine the value of the Hamiltonian at which resonance overlap occurs and hence provide an estimate for the onset of widespread chaos. In figure 14 we plot in the space of the original action variables (I_a, I_b) the resonance conditions (6.3) and (6.4) (curves a_1 and b_1), the boundaries of resonance zone (6.12) and (6.15) (curves a_2 and b_2), and the curves of constant $\mathscr{H}_0$ for the cases of $h = 1.6$, $l = 0.248062$, $\epsilon = 0.009072$ and $\lambda = 0.1$, 0.15, 0.2, 0.3. Superposing the two resonance zones, we obtain the overlap region as shown by the shaded areas in the figures. The global behaviour of the Poincaré sections in figures 12 and 13 can be completely explained in terms of these resonance overlap diagrams.

From figure 14(*a*) for $\lambda = 0.1$, we see that the level curve of $\mathscr{H}_0 \approx \mathscr{H} = 2.0$ does not intersect the resonance overlap zone. This suggests that isolated resonance zones dominate at this low energy and we should see only regular motions, as figure 12(*a*) shows. As $\mathscr{H}_0$ is increased, part of the level curves sweep across the interior of the resonance overlap regime, indicating the onset of chaotic motion. Figure 12(*b*) shows the Poincaré section of such an energy level, $\mathscr{H} = 4.0$, where a chaotic region is seen between the inner and outer regular phase portraits. As the energy level is further raised, the level curves no longer intersect the overlap region and regular motions become predominant again in the phase space as shown in figure 12(*c*) for $\mathscr{H} = 6.0$. This explains the so called banded-energy phenomenon.

The critical-energy phenomenon for $\lambda = 0.2$ with the energy levels of $\mathscr{H}_0 \approx \mathscr{H} =$ 8.0, 9.0, 10.0 and 11.968215 as presented in figure 13 can also be predicted according to the resonance overlap diagram figure 14(*c*). That the phase portraits in figure 13(*a*) are completely regular can be seen from figure 14(*c*) where the level curve of $\mathscr{H}_0 \approx \mathscr{H} = 8.0$ is away from the overlap zone. As the energy level is raised beyond a critical value the level curves never leave the overlap region once they are inside. This corresponds to the critical-energy phenomenon we have seen in the numerical experiments. The phase space will be dominated by chaotic trajectories as indicated in figure 13(*b–d*) for energy levels greater than the critical value.

Since the physical parameters are related in a very complicated way to the coefficients in the Hamiltonian system, the resonance overlap diagrams suggest an effective way to search the space of the parameters. One important piece of information from the resonance overlap diagram is the area of the overlap zone which gives a measure of the degree or likelihood of chaotic motions for the specific set of physical parameters. Thus we simply plot the areas of the overlap zones as a function of the changing parameters. As an illustration, we show the variation of the overlap

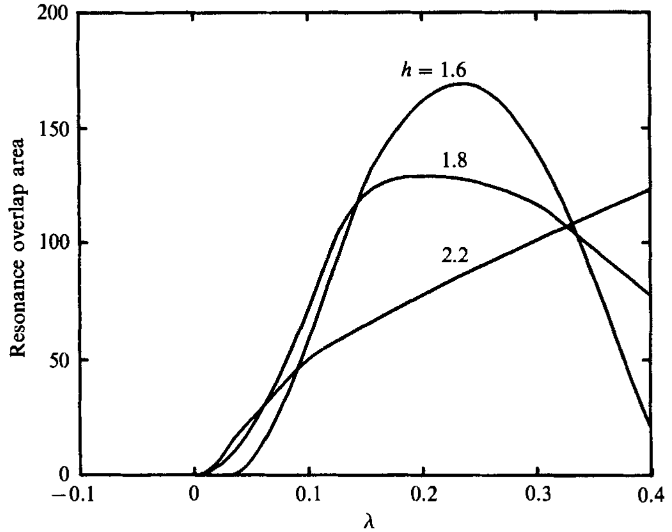

FIGURE 15. Resonance overlap area versus detuning parameter λ for $l = 0.248062$, $\epsilon = 0.009072$ and different values of $h = 1.6$, 1.8 and 2.2.

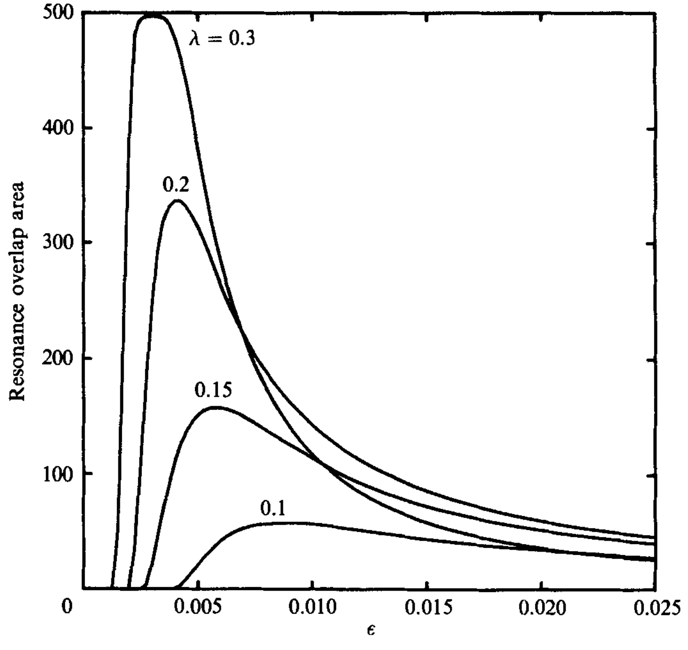

FIGURE 16. Resonance overlap area versus excitation amplitude ϵ for $l = 0.248062$, $h = 1.6$ and different values of $\lambda = 0.1$, 0.15, 0.2 and 0.3.

area with the excitation-frequency detuning parameter λ for $l = 0.248062$, $\epsilon = 0.009072$ and three different depths $h = 1.6$, 1.8 and 2.2 in figure 15. For $h = 2.2$, the overlap area increases monotonically with increasing detuning λ. For the intermediate depths, $h = 1.6$ and 1.8, however, the overlap areas increase to a maximum and then fall off as λ is further increased. The effect of the excitation amplitude ϵ on the degree of chaos can likewise be examined. Figure 16 shows the change of overlap area with ϵ for the cases $l = 0.248062$, $h = 1.6$ and $\lambda = 0.1$, 0.15, 0.2 and 0.3. Surprisingly, the overlap area first increases rapidly for increasing excitation amplitude and then decreases for larger amplitudes so that the most widespread chaotic responses need not be associated with the largest driving amplitudes.

To keep the presentation to a reasonable length, we have not considered the extension to weakly dissipative systems. Such an investigation is now in progress.

This research was supported financially by the National Science Foundation and the Office of Naval Research. Some of the computations were performed on the NSF sponsored Pittsburg Supercomputer Center Cray X/MP. We thank Professor Jack Wisdom for useful discussions.

Appendix. Second-order solution for the internal interaction system

The solutions Φ_2 and ζ_2 for the second-order boundary-value problem of the internal interaction case are

$$\begin{aligned}\Phi_2 = {} & \mathrm{i}(\mathrm{e}^{-\mathrm{i}2t} - \text{c.c.}\left[\sum_{\substack{m=0\\ m\neq n}}^{\infty} d_m \cos m\pi x \cosh m\pi(z+h) - \varphi(x,z)\right] \\ & + \mathrm{i}[A^2\,\mathrm{e}^{-\mathrm{i}(4+2\gamma\epsilon^{\frac{1}{2}})\,t} - \text{c.c.}]\left[a_0 + a_1 \cos 2n\pi x \frac{\cosh 2n\pi(z+h)}{2n\pi \sinh 2n\pi h}\right] \\ & + \mathrm{i}[B^2\,\mathrm{e}^{-\mathrm{i}2t} - \text{c.c.}]\left[b_0 + b_1 \cos 2l\pi y \frac{\cosh 2l\pi(z+h)}{2l\pi \sinh 2l\pi h}\right] \\ & + \mathrm{i}[(AB\,\mathrm{e}^{-\mathrm{i}(3+\gamma\epsilon^{\frac{1}{2}})\,t} - \text{c.c.})\,a_2 + (AB^*\,\mathrm{e}^{-\mathrm{i}(1+\gamma\epsilon^{\frac{1}{2}})\,t} - \text{c.c.})\,b_2] \\ & \times\left[\cos m\pi x \cos l\pi y \frac{\cosh[(n^2+l^2)^{\frac{1}{2}}\pi(z+h)]}{(n^2+l^2)^{\frac{1}{2}}\pi \sinh[(n^2+l^2)^{\frac{1}{2}}\pi h]}\right] \\ & + (AA^*)\,a_3\,t + (BB^*)\,b_3\,t, \end{aligned} \tag{A 1}$$

and

$$\begin{aligned}\zeta_2 = {} & -\frac{2}{\mu}(\mathrm{e}^{-\mathrm{i}2t} + \text{c.c.})\left[\sum_{\substack{m=0\\ m\neq n}}^{\infty} d_m \cos m\pi x \cosh m\pi h - \varphi(x,0)\right] \\ & -\frac{1}{\mu}(\mathrm{e}^{-\mathrm{i}2t} + \text{c.c.})\,(f_n - \tfrac{1}{4}\mu f'_n) \cos m\pi x \\ & - \mathrm{i}\lambda[A\,\mathrm{e}^{-\mathrm{i}(2+\gamma\epsilon^{\frac{1}{2}})\,t} - \text{c.c.}] \cos m\pi x - \mathrm{i}\lambda(B\,\mathrm{e}^{-\mathrm{i}t} - \text{c.c.}) \cos l\pi y \\ & - [A^2\,\mathrm{e}^{-\mathrm{i}(4+2\gamma\epsilon^{\frac{1}{2}})\,t} + \text{c.c.}]\,\tilde{a}_1 \cos 2n\pi x - [B^2\,\mathrm{e}^{-\mathrm{i}2t} + \text{c.c.}]\,\tilde{b}_1 \cos 2l\pi y \\ & - [(AB\,\mathrm{e}^{\mathrm{i}(3+\gamma\epsilon^{\frac{1}{2}})\,t} + \text{c.c.})\,\tilde{a}_2 + (AB^*\,\mathrm{e}^{-\mathrm{i}(1+\gamma\epsilon^{\frac{1}{2}})\,t} + \text{c.c.})\,\tilde{b}_2] \cos n\pi x \cos l\pi y \\ & - (AA^*)\,\tilde{a}_3 \cos 2n\pi x - (BB^*)\,\tilde{b}_3 \cos 2l\pi y, \end{aligned} \tag{A 2}$$

where

$$a_0 = -\tfrac{1}{256}(n^2\pi^2\mu^2 + 48), \quad b_0 = -\tfrac{1}{32}(3 + \mu_y^2\, l^2\pi^2),$$

$$a_1 = \frac{n^2\pi^2\mu}{256}(3n^2\pi^2\mu^2 - 48), \quad b_1 = -\tfrac{3}{8}\mu_y\, l^2\pi^2(1 - \mu_y^2\, l^2\pi^2),$$

$$a_2 = \frac{(n^2+2l^2)\,\pi^2\mu^2 - 42}{72\tilde{\mu} - 8\mu}, \quad b_2 = \frac{(2l^2 - n^2)\,\pi^2\mu^2 + 6}{8\tilde{\mu} - 8\mu},$$

$$a_3 = \tfrac{1}{32}(16 - n^2\pi^2\mu^2), \quad b_3 = \tfrac{1}{8}(1 - \mu_y^2\, l^2\pi^2),$$

$$\tilde{a}_1 = \frac{n^2\pi^2\mu}{1024}(3n^2\pi^2\mu^2 - 16), \quad \tilde{b}_1 = \tfrac{1}{16}\mu_y\, l^2\pi^2(1 - 3\mu_y^2\, l^2\pi^2),$$

$$\tilde{a}_2 = \frac{l^2\pi^2\mu}{16}(3l^2\pi^2\mu^2 - 1), \quad \tilde{b}_2 = \frac{(2l^2 - n^2)\,\pi^2\mu\tilde{\mu} + 6}{8\tilde{\mu} - 8\mu},$$

$$\tilde{a}_3 = \frac{3(n^2 + 2l^2)\,\pi^2\mu\tilde{\mu} - 14}{8\tilde{\mu} - 8\mu}, \quad \tilde{b}_3 = \frac{1}{8\mu_y}(1 + \mu_y^2\, l^2\pi^2),$$

$$d_0 = -\frac{h^2}{24} - \frac{\mu_y h}{8}, \quad d_m = \frac{4 + m\pi\mu_y \tanh m\pi h - \dfrac{8}{m\pi h}\tanh \tfrac{1}{2}m\pi h}{m^2\pi^2(m\pi\mu_y \sinh m\pi h - 4\cosh m\pi h)},$$

and

$$\tilde{\mu} = \frac{1}{(n^2 + l^2)^{\frac{1}{2}}\pi \tanh (n^2 + l^2)^{\frac{1}{2}}\pi h}.$$

REFERENCES

ARNOL'D, V. I. 1978 *Mathematical Methods of Classical Mechanics.* Springer.

BENJAMIN, T. B. & FEIR, J. E. 1967 The disintegration of wave trains in deep water. Part 1. Theory. *J. Fluid Mech.* **27**, 417–430.

BENETTIN, G., GALGANI, L. & STRELCYN, J. M. 1976 Kolmogorov entropy and numerical experiments. *Phys. Rev.* **A14**, 2338–2345.

CHIRIKOV, B. 1979 A universal instability of many dimensional oscillation systems. *Phys. Rep.* **52**, 263–379.

CILIBERTO, S. & GOLLUB, J. P. 1984 Pattern competition leads to chaos. *Phys. Rev. Lett.* **52**, 922–925.

CILIBERTO, S. & GOLLUB, J. P. 1985*a* Chaotic mode competition in parametrically forced surface waves. *J. Fluid Mech.* **158**, 381–398.

CILIBERTO, S. & GOLLUB, J. P. 1985*b* Phenomenological model of chaotic mode competition in surface waves. *Il Nuovo Cimento* **6D**, 309–316.

FENG, Z. C. & SETHNA, P. R. 1989 Symmetry-breaking bifurcations in resonant surface waves. *J. Fluid Mech.* **199**, 495–518.

FULTZ, D. 1962 An experimental note on finite-amplitude standing gravity waves. *J. Fluid Mech.* **13**, 193–212.

FUNAKOSHI, M. & INOUE, S. 1987 Chaotic behaviour of resonantly forced surface water waves. *Phys. Lett.* **A121**, 229–232.

FUNAKOSHI, M. & INOUE, S. 1988 Surface waves due to resonant horizontal oscillation. *J. Fluid Mech.* **192**, 219–247.

GARRETT, C. J. R. 1970 On cross-waves. *J. Fluid Mech.* **41**, 837–849.

GOLLUB, J. P. & MEYER, C. W. 1983 Symmetry-breaking instabilities on a fluid surface. *Physica* **6D**, 337–346.

GU, X. M. & SETHNA, P. R. 1987 Resonant surface waves and chaotic phenomenon. *J. Fluid Mech.* **183**, 543–565.

HAVELOCK, T. H. 1929 Forced surface-waves on water. *Phil. Mag.* **8**, 304–311.

KEOLIAN, R., TURKEVICH, L. A., PUTTERMAN, S. J. & RUDNICK, I. 1981 Subharmonic sequences in the Faraday experiment: Departures from period doubling. *Phys. Rev. Lett.* **47**, 1133–1136.

LIN, J. N. & HOWARD, L. N. 1960 Non-linear standing waves in a rectangular tank due to forced oscillation. *MIT Hydrodynamics Laboratory, Rep.* 44.

MERON, E. & PROCACCIA, I. 1986*a* Theory of chaos in surface waves: The reduction from hydrodynamics to few-dimensional dynamics. *Phys. Rev. Lett.* **56**, 1323–1326.

MERON, E. & PROCACCIA, I. 1986*b* Low-dimensional chaos in surface waves: Theoretical analysis of an experiment. *Phys. Rev.* **A34**, 3221–3237.

MERON, E. & PROCACCIA, I. 1987 Gluing bifurcations in critical flows: The route to chaos in parametrically excited surface waves. *Phys. Rev.* **A35**, 4008–4011.

MILES, J. W. 1984*a* Nonlinear Faraday resonance. *J. Fluid Mech.* **146**, 285–302.

MILES, J. W. 1984*b* Resonantly forced surface waves in a circular cylinder. *J. Fluid Mech.* **149**, 15–31.

MILES, J. W. 1988 Parametrically excited, standing cross-waves. *J. Fluid Mech.* **186**, 119–127.

NAYFEH, A. H. 1987 Surface waves in closed basins under parametric and internal resonances. *Phys. Fluids* **30**, 2976–2983.

PENNEY, W. G. & PRICE, A. T. 1952 Some gravity wave problem in the motion of perfect liquids. Part II. Finite periodic stationary gravity waves in a perfect liquid. *Phil. Trans. R. Soc. Lond.* A **244**, 254–284.

SHEMER, L. & KIT, E. 1988 Study of the role of dissipation in evolution of nonlinear sloshing waves in a rectangular channel. *Fluid Dyn. Res.* **4**, 89–105.

SIMONELLI, F. & GOLLUB, J. P. 1989 Surface wave mode interactions: effects of symmetry and degeneracy. *J. Fluid Mech.* **199**, 471–494.

STRUBLE, R. A. 1963 Oscillations of a pendulum under parametric excitation. *Q. Appl. Maths* **21**, 121–131.

TABOR, M. 1981 The onset of chaotic motion in dynamical systems. *Adv. Chem. Phys.* **46**, 73–151.

TADJBAKHSH, I. & KELLER, J. B. 1960 Standing surface waves of finite amplitude. *J. Fluid Mech.* **8**, 442–451.

TSAI, W. T. & YUE, D. K. P. 1988 Nonlinear standing waves in a two-dimensional heaving tank. *Proc. 3rd Intl Workshop Water Waves & Floating Bodies*, pp. 163–167. Woods Hole.

UMEKI, M. & KAMBE, T. 1989 Nonlinear dynamics and chaos in parametrically excited surface waves. *J. Phys. Soc. Japan* **58**, 140–154.

URSELL, F., DEAN, R. G. & YU, Y. S. 1959 Forced small-amplitude water waves: a comparison of theory and experiment. *J. Fluid Mech.* **7**, 33–52.

ZUFIRIA, J. 1988 Oscillatory spatially periodic weakly nonlinear gravity waves on deep water. *J. Fluid Mech.* **191**, 341–372.